Ocean Science

TOPAZ4: an ocean-sea ice data assimilation system for the North Atlantic and Arctic

P. Sakov[1,2], **F. Counillon**[1,3], **L. Bertino**[1,3], **K. A. Lisæter**[4], **P. R. Oke**[2], **and A. Korablev**[1]

[1]Nansen Environmental and Remote Sensing Center, Bergen, Norway
[2]CSIRO Marine and Atmospheric Research, Hobart, Australia
[3]Bjerknes Centre for Climate Research, Bergen, Norway
[4]Storm Geo AS, Bergen, Norway

Correspondence to: P. Sakov (pavel.sakov@gmail.com)

Abstract. We present a detailed description of TOPAZ4, the latest version of TOPAZ – a coupled ocean-sea ice data assimilation system for the North Atlantic Ocean and Arctic. It is the only operational, large-scale ocean data assimilation system that uses the ensemble Kalman filter. This means that TOPAZ features a time-evolving, state-dependent estimate of the state error covariance. Based on results from the pilot MyOcean reanalysis for 2003–2008, we demonstrate that TOPAZ4 produces a realistic estimate of the ocean circulation in the North Atlantic and the sea-ice variability in the Arctic. We find that the ensemble spread for temperature and sea-level remains fairly constant throughout the reanalysis demonstrating that the data assimilation system is robust to ensemble collapse. Moreover, the ensemble spread for ice concentration is well correlated with the actual errors. This indicates that the ensemble statistics provide reliable state-dependent error estimates – a feature that is unique to ensemble-based data assimilation systems. We demonstrate that the quality of the reanalysis changes when different sea surface temperature products are assimilated, or when in-situ profiles below the ice in the Arctic Ocean are assimilated. We find that data assimilation improves the match to independent observations compared to a free model. Improvements are particularly noticeable for ice thickness, salinity in the Arctic, and temperature in the Fram Strait, but not for transport estimates or underwater temperature. At the same time, the pilot reanalysis has revealed several flaws in the system that have degraded its performance. Finally, we show that a simple bias estimation scheme can effectively detect the seasonal or constant bias in temperature and sea-level.

1 Introduction

TOPAZ4 is the latest version of TOPAZ, a coupled ocean-sea ice data assimilation (DA) system for the North Atlantic Ocean and Arctic (Fig. 1). It emerged in 2007–2010 following the development of TOPAZ3 (Bertino and Lisæter, 2008), and represents the main workhorse of the Arctic Marine Forecasting Center (MFC) of the MyOcean project (http://www.myocean.eu.org) both for short-term forecasting and reanalysis purposes.

The system is based on an ensemble Kalman filter (EnKF) (Evensen, 1994) with a 100-member ensemble. It uses the hybrid coordinate ocean model (HYCOM, e.g. Bleck, 2002; Chassignet et al., 2006) coupled with a sea-ice model (Hunke and Dukowicz, 1997). Compared to TOPAZ3, TOPAZ4 has undertaken a number of substantial modifications in the DA scheme, the model, and the system configuration. These modifications are detailed in the following sections of the paper.

TOPAZ is the only operational, large-scale, eddy-resolving ocean DA system that uses the EnKF. This contrasts from numerical weather prediction (NWP), where there are currently a number of operational, or semi-operational, EnKF systems (Houtekamer and Mitchell, 2006; Torn and Hakim, 2008; Bonavita et al., 2008; Compo et al., 2011). Ocean forecasting differs from NWP in several respects. Apart from the differences in the number of observations available – the ocean observing system is much sparser than the atmospheric observing system – the ocean and atmosphere vary on different spatial and temporal scales. Ocean variability is dominated by mesoscale eddies that vary on
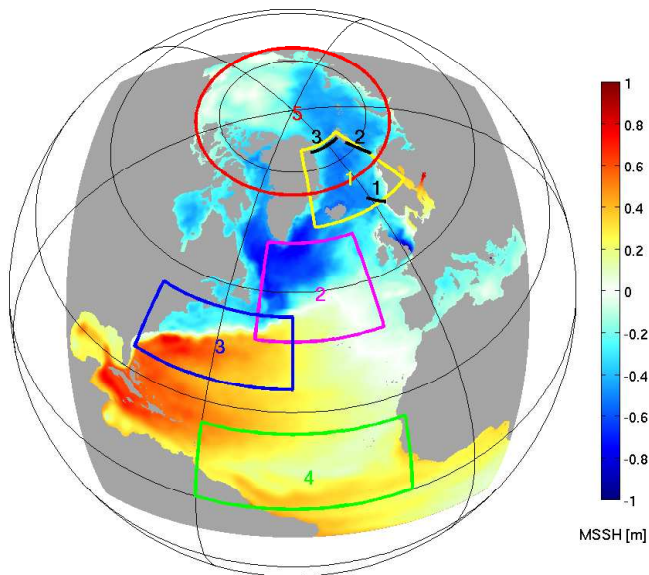
Fig. 1. TOPAZ model domain. The background colour shows the mean sea surface height computed from a free model run over the period 1993–1999; the grey colour shows land; the numbered boxes show regions used for calculating innovation statistics for the re-analysis (see Table 2); and the black lines show the sections used for volume transport and temperature validation: Svinoy section (1); Barents Sea Opening section (2); and Fram Strait section (3).

Fig. 2. Example of correlation between ICEC at a location close to the ice edge (marked "+") and sea surface salinity. Calculated from TOPAZ ensemble in the course of the reanalysis for a location in Barents Sea on 27 June 2007. The green contour line corresponds to ICEC of 0.2 (20 %); the area to the left of it is covered by ice, while the area to the right is ice free. Land cells are shown in grey colour.

spatial scales of 50–200 km at mid-latitudes and on time-scales of days to weeks. By contrast, atmospheric variability is dominated by weather systems that vary on larger spatial scales of 1000 km, or greater, and often on time-scales of hours. As a consequence, large-scale eddy-resolving ocean models are often several times larger than their atmospheric counterparts. Running an EnKF for a large-scale, eddy-resolving ocean model is therefore often prohibitively expensive. Perhaps as a direct result of this, most large-scale, eddy-resolving ocean forecast systems use a single deterministic forecast, together with either a variant of Ensemble Optimal Interpolation (EnOI; Oke et al., 2010), where the background error covariance is approximated by a time-invariant ensemble (Oke et al., 2008) or a seasonally varying ensemble (Brasseur et al., 2005); or a statistical DA scheme, like Optimal Interpolation (OI; Chassignet et al., 2007, see Cummings et al., 2009, for a review). Srinivasan et al. (2011) compare these methods in a twin experiment and show that they yield a similar performance. Because TOPAZ is under-pinned by a regional ocean model, rather than a global model, a full EnKF was deemed affordable.

In this paper we argue that having the time dependent state error covariance is essential for DA in a coupled ice-ocean system. Compared to DA in the open ocean without sea-ice, this system is characterised by strong anisotropy and non-stationarity caused by the presence of the ice edge (Lisæter et al., 2003). To demonstrate this, Fig. 2 shows a typical
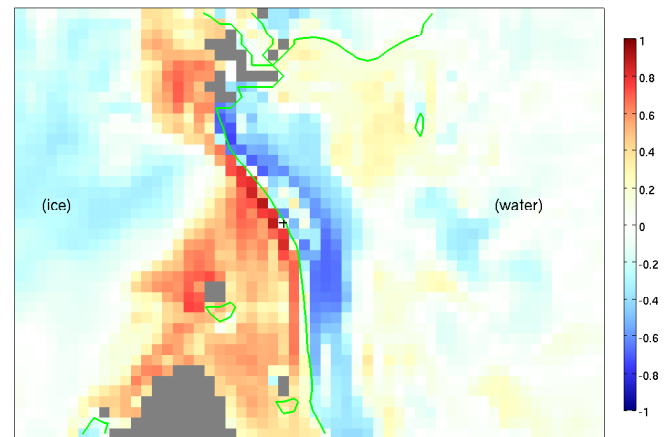
correlation pattern between ice concentration (ICEC) at the ice edge and sea surface salinity (SSS) elsewhere during the melting season. The correlation field in Fig. 2 shows the ensemble-derived influence of an observation of ice concentration at the reference location (denoted in the figure) with SSS state in the surrounding region for a particular instance in time. The correlation field is strongly anisotropic. It is positive in the ice covered areas, corresponding to the freshening of the water as the ice melts; but it is negative in the ice-free areas, where the state of the the ice is driven by the advection of warm and saline Atlantic water. This field is also non-stationary owing to the constant movement of the ice edge caused by wind-driven advection and melting/freezing of the ice. The pattern shown is characteristic of the melting season; at other times it can be monopole (with negative correlations; not shown), or have close to zero correlations (not shown). Because of the non-stationarity and anisotropy of the physical system, DA systems with stationary background covariances (3D-Var, 4D-Var, EnOI) are unlikely to yield a physically sensible analysis after assimilation of the ICEC observations.

The outline of this paper is as follows. Details of the model are presented in Sect. 2, followed by a description of the DA system in Sect. 3; the configuration of a 6-year reanalysis in Sect. 4; an evaluation of the reanalysis results in Sect. 5; and the conclusions in Sect. 6.

2   The model

TOPAZ4 uses version 2.2 of HYCOM. In our implementation of HYCOM, the vertical coordinate is isopycnal in the

stratified open ocean and z-coordinates in the unstratified surface mixed layer. Isopycnal layers permit high resolution in areas of strong density gradients and better conservation of tracers and potential vorticity; and z-layers are well suited to regions where surface mixing is important. To realistically simulate the circulation in the Arctic region, an ocean model requires a particularly accurate representation of the dense overflow and the surface mixed layer to isolate the warm Atlantic inflow from the sea ice. In our opinion this makes HYCOM a suitable model for the North Atlantic and Arctic region that spans the stratified open ocean, a wide continental shelf, regions of steep topography, and extensive sea ice. HYCOM also permits sigma coordinates that can be beneficial in coastal regions, however, we have not adopted this option here because coastal areas are not our prior objective.

Compared to TOPAZ3 (Bertino and Lisæter, 2008), the model has been modified for simulating better the different water masses in the Arctic. Modifications include higher vertical resolution to improve the inflow of Atlantic Water, fine tuning of the model parameters for viscosity and diffusion, and improvement of the methodology employed for surface relaxation (see below). The model uses biharmonic viscosity ($0.2\,kg\,m^{-1}\,s^{-1}$), biharmonic velocity diffusion ($0.06\,m\,s^{-1}$), and spatially varying layer thickness diffusion (of $0.06\,m\,s^{-1}$ in the Gulf Stream region and smooth transit to 0.01 elsewhere). Also, improved river run-off and the inclusion of transport through the Bering Strait improve the inflow of fresh water into the Arctic.

The TOPAZ4 implementation of HYCOM uses: the tracer and continuity equation solved with the second order flux corrected transport (FCT2, Iskandarani et al., 2005; Zalesak, 1979); the turbulent mixing sub-model from the Goddard Institute for Space Studies (Canuto et al., 2002); the vertical remapping for fixed and non-isopycnal coordinate layers with the Weighted Essentially Non-Oscillatory (WENO) piecewise parabolic scheme; the short wave radiation penetration with varying exponential decay depending on the Jerlov water type (Halliwell, 2004); and biharmonic viscosity.

The model is coupled to a one thickness category sea-ice model with elastic-viscous-plastic (EVP) rheology (Hunke and Dukowicz, 1997); its thermodynamics are described in Drange and Simonsen (1996) with a correction of heat fluxes for sub-grid scale ice thickness heterogeneities following Fichefet and Morales Maqueda (1997). The sea-ice strength is set to $27\,500\,N\,m^{-2}$. The advection of ice concentration, ice thickness, snow depth, first year ice fraction and ice age is calculated using a 3rd order WENO scheme (Jiang and Shu, 1996), with a 2nd order Runge-Kutta time discretisation.

The model domain covers the North Atlantic and Arctic basins (see Fig. 1), with the horizontal model grid created by a conformal mapping with the poles shifted to the opposite side of the globe to achieve a quasi-homogeneous grid size (Bentsen et al., 1999). The grid has 880×800 horizontal grid points, with approximately 12–16 km grid spacing in the whole domain. This is eddy-permitting resolution for low and middle latitudes, but is too coarse to properly resolve all of the mesoscale variability in the Arctic, where the Rossby radius is as small as 1–2 km.

The model uses 28 hybrid layers with carefully chosen reference potential densities of 0.1, 0.2, 0.3, 0.4, 0.5, 24.05, 24.96, 25.68, 26.05, 26.30, 26.60, 26.83, 27.03, 27.20, 27.33, 27.46, 27.55, 27.66, 27.74, 27.82, 27.90, 27.97, 28.01, 28.04, 28.07, 28.09, 28.11, 28.13[1]. The top five target densities are purposely low to force them to remain z-coordinates. The minimum z-level thickness of the top layer is 3 m, while the maximum z-layer thickness is 450 m, to resolve the deep mixed layer in the Sub-Polar Gyre and Nordic Seas. The model bathymetry is interpolated from the General Bathymetric Chart of the Oceans database (GEBCO) at 1-min resolution.

The model is initialised in 1973 using climatology that combines the World Atlas of 2005 (WOA05, Locarnini et al., 2006; Antonov et al., 2006) with version 3.0 of the Polar Science Center Hydrographic Climatology (PHC, Steele et al., 2001). At the lateral boundaries, model fields are relaxed towards the same monthly climatology, with the relaxation zone width of 20 grid cells and an e-folding time of 30 day MLD/15 m. The model includes an additional barotropic inflow of 0.7 Sv through the Bering Strait, representing the inflow of Pacific Water. This inflow is balanced by an outflow at the southern boundary of the domain in the Atlantic Ocean. Although the seasonal variability of the Bering Strait transport is not considered, it seems to have a rather limited impact on the circulation (Ness et al., 2010; Wadley and Bigg, 2002).

For the reanalysis experiment presented in this paper, TOPAZ is forced at the ocean surface with fluxes derived from 6-hourly reanalysed atmospheric fluxes from ERA-interim (Dee et al., 2011). The atmospheric fields from ERA-interim include: precipitation, dew point temperature, total cloud cover, air temperature at 2 m, sea level pressure, wind speed at 10 m and long wave radiation at the sea surface. The thermodynamic fluxes are computed as in Drange and Simonsen (1996), but the cloud cover fields are updated every 3 h in the computation of the shortwave radiation to better represent the diurnal cycle. The momentum flux is computed as in Large and Pond (1981). The surface fluxes are forced with a bulk formula parametrisation (Kara et al., 2000).

The value of river discharge is poorly known because the observation array for river flows is sparse. A monthly climatological discharge is estimated by applying the run-off estimates from ERA-interim to the Total Runoff Integrating Pathways (TRIP, Oki and Sud, 1998) over the 20-year reanalysis period (1989–2009). As in most models, the remaining inaccuracies in the precipitation, evaporation and run-off are constrained using surface relaxation of salinity towards monthly climatology. We only use this relaxation

---

[1]One needs to add 1000 to obtain the volumic mass in $kg\,m^{-3}$

in open ocean areas. The settings are described in Chassignet et al. (2007). This relaxation probably removes part of the interannual variability, but is unavoidable considering the uncertainties in freshwater fluxes. However, relaxation can have a detrimental impact on some regions – particularly where strong fronts occur and/or they are misplaced (e.g. Gulf Stream). In such places the water mass distribution is bimodal, and the relaxation towards an average estimate reduces the sharpness of fronts. To avoid this problem, relaxation is only activated when the difference between the climatology and the model is less than 0.5 PSU (M. Bentsen personal communication, 2010).

The diagnosed model SSH is the steric height anomaly that varies due to barotropic pressure mode, deviations in temperature and salinity, and does not include the inverse barometer effect (atmospheric effect). The model mean SSH is computed over the period 1993–1999 and used to assimilate altimeter observations (see Fig. 1).

The model code is publicly available. It can be accessed from https://svn.nersc.no/repos/hycom or browsed at https://svn.nersc.no/hycom/browser.

3 Data assimilation

3.1 The scheme and general settings

TOPAZ4 has transitioned from using the traditional "perturbed observations" EnKF scheme (Burgers et al., 1998) to the "deterministic EnKF", or DEnKF, that was developed by Sakov and Oke (2008a). In the case of "weak" DA, when the increments are much smaller than the ensemble spread, the DEnKF is asymptotically equivalent to the symmetric right multiplied ensemble square root filter (ESRF) (Sakov and Oke, 2008b), commonly known as the ETKF (Bishop et al., 2001). In the case of "strong" DA, the DEnKF yields smaller increments than the ESRF – a characteristic that can be interpreted as adaptive inflation, aimed at increasing the robustness of the system.

Similar to TOPAZ3, TOPAZ4 uses a simple, non-adaptive, distance-based localisation method known as "local analysis" (Evensen, 2003; Sakov and Bertino, 2011). With this method, a local analysis is computed for one horizontal grid point at a time, using observations from a spatial window around it. In contrast to TOPAZ3, TOPAZ4 uses smooth localisation (rather than a box-car type localisation) that yields spatially continuous analyses. The smoothing is implemented by multiplying local ensemble anomalies, or perturbations, by a quasi-Gaussian, isotropic, distance dependent localisation function (Gaspari and Cohn, 1999). The localisation radius, beyond which the ensemble-based covariance between two points is artificially reduced to zero, is uniform in space and is set to 300 km. This corresponds to an $e^{1/2}$-folding radius of about 90 km.

During each analysis step, TOPAZ calculates a 100×100 local ensemble transform matrix (ETM, called $\mathbf{X}_5$ in Evensen, 2003) for each of the 880×800 horizontal model grid cells. The matrix inversion involved in the calculation of each local ETM is performed either in ensemble or observation space (whichever is smaller), depending on whether the number of locally assimilated observations is greater than or smaller than the ensemble size. This 880×800 array of ETMs is then used for updating each horizontal model field (about 150 fields total).

The analysis is performed in the model grid space. The instances of negative layer thickness or ice concentration, should they occur, are corrected in a post-processing procedure. The next cycle is restarted from the analysis in a straightforward manner; without using incremental update or nudging.

The DA code is publicly available. It can be accessed from https://svn.nersc.no/repos/enkf or browsed at https://svn.nersc.no/enkf/browser.

3.2 Moderation of observation errors

Several aspects of the practical implementation of TOPAZ4 are designed to make the system's performance more robust. Examples of these, described above, include the use of localisation and the calculation of local analyses, instead of global analyses. Another aspect of the implementation that makes the DA more robust is the estimation of observation errors. In practice, we inflate the assumed observation error variance when we update the ensemble anomalies. Recall that the update of the model state in the Kalman filter can be derived from balancing the first order terms in the cost function, while the update to state error covariance can be derived from balancing the second order terms (Hunt et al., 2007). Therefore, a relatively small error in the system can have a minor effect on the update of the ensemble mean, but a much more significant effect on the update of the ensemble anomalies. Because it is important for the robustness of the system to ensure that the variance is bigger rather than smaller, we consider it prudent to use a weaker update for the state error covariance. For the reanalysis presented here we use an observation error variance that is increased by a factor of 2 for updating the ensemble anomalies, while the original observation error variance is used for updating the ensemble mean.

Another moderation technique can be characterised as an adaptive observation pre-screening. If for some reason the innovation associated with an observation is too large compared to the forecast error, assimilation of this observation is likely to produce a physically unbalanced analysis. In such a case, the large magnitude of the innovation may not be due to a rogue observation. It may occur because of errors in the forcing, or if there are insufficient observations to properly constrain the model. In such situations it may be better to limit the impact from the observation rather than to discard

Table 1. Overview of observations used in the reanalysis. Notes: [1] before 1 April 2006; [2] after 1 April 2006; [3] after 18 April 2007.

Type	Product or Provider	Number	After SO	Spatial type	Asynch.
SLA	CLS	9×10^4	4×10^4	Track	Yes
SST[1]	Reynolds	6×10^3	"	Gridded	No
SST[2]	OSTIA	2×10^6	2.2×10^5	Gridded	No
In-situ T	Argo (Ifremer) + other[3]	$2 \times 10^4 + 1.5 \times 10^{4\,[3]}$	6×10^3	Point	No
In-situ S	Argo (Ifremer) + other[3]	$2 \times 10^4 + 1.5 \times 10^{4\,[3]}$	6×10^3	Point	No
ICEC	AMSR-E	1.6×10^5	10^5	Gridded	No
Ice drift	CERSAT	6×10^3	"	Gridded	Yes
Total		2.3×10^6	4×10^5		

it altogether. In TOPAZ, all assimilated observations are pre-screened against the ensemble spread in observation space, and their error variance is modified smoothly in such way that its magnitude is limited to twice the ensemble spread:

$$\tilde{\sigma}_{\text{obs}}^2 = \sqrt{(\sigma_{\text{ens}}^2 + \sigma_{\text{obs}}^2)^2 + \left(\frac{1}{K}\,\sigma_{\text{ens}}\,\delta d\right)^2} - \sigma_{\text{ens}}^2,$$

where $\tilde{\sigma}_{\text{obs}}^2$ is the modified value of observation error variance; σ_{obs}^2 is the original observation error variance; $\sigma_{\text{ens}}^2 = \mathbf{H}\mathbf{P}^f\mathbf{H}^{\mathrm{T}}$ is the corresponding estimate of the state error variance; δd is the innovation (observation minus observation forecast); and K is the maximal allowed magnitude of the increment for the observational variable expressed in terms of σ_{ens}: $|\mathbf{H}(\mathbf{x}^a - \mathbf{x}^f)| \leq K\sigma_{\text{ens}}$ (set to $K = 2$). This procedure normally has a negligible impact on the system, but does prevent an excessive shock that can occur if the model and the observations happen to be too far apart.

3.3 The perturbation system

The model perturbation system is a critically important part of TOPAZ. It accounts for the model error by increasing the model spread through perturbation of a number of forcing fields. Perturbing model states indirectly through the forcing fields ensures their dynamic consistency.

The perturbation system currently used in TOPAZ was initially taken from Brusdal et al. (2003) and then was adapted empirically after years of operational runs. The perturbations of the forcing fields are assumed to be red noise simulated by the spectral method described by Evensen (2003). The perturbations are computed in a Fourier space with a decorrelation time-scale of 2 days and horizontal decorrelation length scale of 250 km. We perturb air temperature, with the standard deviation of 3 °C; cloud cover (20 %); and per-area precipitation flux $(4 \times 10^{-9}\,\text{m s}^{-1})^2$. The perturbations of the wind field are derived from sea level pressure (SLP) pertur-

bations, which have a standard deviation of 3.2 mb decorrelation lengths and time scale identical to the previous perturbations. The wind perturbations are the geostrophic winds related to the SLP perturbations, their intensity being inversely proportional to the value of the Coriolis parameter. At 40° N the standard deviations of the winds is $1.5\,\text{m s}^{-1}$. The wind perturbations transition smoothly from 15° to the Equator, where they are aligned with the gradients of SLP perturbations. In order to increase the ensemble spread in sea ice, the squared parameter e in the EVP rheology (Hunke and Dukowicz, 1997, Table 1) is perturbed. This parameter represents the ratio between the minor and the major axis of the elliptic yield curve, which partly controls the transition between the viscous and plastic flows for a given stress. In other words, it represents the shear to compression strength ratio. The optimal value for this parameter is poorly known and may vary with time and space (Dumont et al., 2009). To perturb e^2, a Gamma distribution is used ($k = 5$, $\sigma = 1$, D. Dumont, personal communication, 2010).

3.4 Diagnostics

A number of diagnostic variables are routinely calculated in TOPAZ4 during the analysis. Firstly, the data for each (super)observation[3] assimilated is saved to permit easy access to the innovation statistics. This includes the forecast and estimated forecast error variance, observations assimilated and the assumed observation error variance, the increment, and the coordinates. Secondly, estimates of degrees of freedom of signal, or DFS (Rodgers, 2000; Cardinali et al., 2004) are calculated in each local analysis, both total and for each observation data type, and stored as a 2-dimensional field. Thirdly, a theoretical estimate for the spread reduction factor, or SRF, is also calculated, both total and for each observation type.

---

[2]Prior to April 2007, these values were 3 °C, 7 % and $0\,\text{m s}^{-1}$, respectively.

[3]A super-observation is an observation combined from a number of primary observations prior to data assimilation. It usually involves primary observations of similar type within the same model cell. The process of combining observations into super-observations is often referred to as superobing. Its purpose is to reduce the number of assimilated observations.

The DFS and SRF are two different metrics that can be calculated from the SVD spectra of the forecast and analysis state error covariance. While the use of DFS for diagnostics of the impact of observations in DA is rather common, SRF, to the best of our knowledge, is a new metric. It is related to the reduction of the state error variance (or, in the context of the EnKF, to the reduction of the ensemble spread) during the analysis, and can been used to characterise the "strength" of assimilation Sakov and Bertino (2011, p. 230). The SRF is defined as

$$\mathrm{SRF} = \left[\frac{\mathrm{trace}(\mathbf{H}\mathbf{P}^f\mathbf{H}^\mathrm{T}\mathbf{R}^{-1})}{\mathrm{trace}(\mathbf{H}\mathbf{P}^a\mathbf{H}^\mathrm{T}\mathbf{R}^{-1})} \right]^{1/2} - 1,$$

where $\mathbf{P}^f$ and $\mathbf{P}^a$ are the forecast and analysis error covariances; $\mathbf{H}$ is the observation matrix; $\mathbf{R}$ is the observation error covariance; and superscript "T" denotes matrix transposition. An SRF value of 0 means no impact from DA, while the value of 1 corresponds to reduction of ensemble spread by a factor of 2 (and a reduction of the estimate for the state error variance by a factor of 4).

Both the DFS and SRF are useful diagnostics of the DA and for assessing the effects on the system from changes in observations or system settings. DFS is a good indicator of potential rank problems. Ideally, one would like to keep it below about 20 for the ensemble size of 100; while values of around 50 would point at too small ensemble or too big localisation radius. SRF characterises the "strength" of data assimilation. "Strong" data assimilation implies a high degree of optimality of the system and should be avoided. Ideally, the magnitude of SRF should not much exceed 1. If SRF is consistently higher than that then perhaps a shorter cycle is needed to limit the growth of unstable modes.

An example of DFS and SRF fields is shown in Fig. 3. Note the difference in the two fields resulting from the difference in how the two metrics are defined: SRF is mostly influenced by changes in a relatively small number of strongly growing modes, while DFS can be affected by changes in a large number of modes, including the weaker ones.

4 Reanalysis

4.1 Generation of the initial ensemble and system spin-up

The initial ensemble is generated so that it contains variability both in the interior of the ocean and at surface. We take 20 random model states from each September of a 20-year model run (1990–2009). Each of these states are used to produce five alternative states by adding spatially correlated noise to the layer and ice thickness, with an amplitude that is 10 % of each field, with a spatial decorrelation length scale of 50 km. The perturbation of isopycnal ocean layer thickness also has a vertical decorrelation scale of three layers,

and an exponential covariance structure. The initial ensemble is integrated for 40 days to damp instabilities that result from dynamical inconsistencies that may be present in the initial perturbations.

After generating the initial ensemble the DA system is spun up during a period of 4 months, for the period from September to December 2002. In order to limit the impact from an abrupt start of DA, the observation error variance is inflated by a factor of 8 at the start of the reanalysis and gradually decreased to the desired level over a period of one year.

4.2 Observations

Observations that are assimilated by TOPAZ4 include along-track Sea Level Anomalies (SLA) from satellite altimeters, Sea Surface Temperature (SST) from the Operational Sea Surface Temperature and Sea Ice Analysis (OSTIA), in-situ temperature and salinity from Argo floats, ICEC from AMSR-E, and sea-ice drift data from CERSAT. The system uses a 7-day assimilation cycle, and assimilates the gridded SST, ICEC and ice drift fields for the day of the analysis; and along-track SLA and in-situ T and S for the week prior to the day of the analysis. A brief overview of observations used in the reanalysis is given in Table 1.

Quality control procedures and preprocessing steps include a range check and horizontal superobing. The details for each observation type follow.

The altimetry data used for assimilation are the along-track SLA from TOPEX/Poséidon, ERS1, JASON-1, JASON-2, ENVISAT provided by Collecte Localisation Satellites (CLS, ftp.aviso.oceanobs.com/global/dt/upd/sla/) from January 1993 to present. These data are geophysically corrected for tides, inverse barometer, tropospheric, and ionospheric signals (Le Traon and Ogor, 1998; Dorandeu and Le Traon, 1999). The oceanographic signal is less accurate near the coast because of pollution by land and in shallow waters due to inaccuracies of the global tidal model that is used to de-alias the along-track altimeter observations. Therefore, we only retain data located both in water deeper than 200 m and at least 50 km away from the coast. The observation error is computed as follows:

$$\sigma_\mathrm{o}^2 = \sigma_\mathrm{instr}^2 + \sigma_\mathrm{repr}^2, \tag{1}$$

where σ_instr is set as recommended by the provider (3 or 4 cm depending on the satellite), and σ_repr is represented by the representation error that accounts for sub-grid variability of observations. Little is known about the latter and we assume that this error is larger in the more dynamical areas (Oke and Sakov, 2008). Thus, a proxy based on the model variance for the period 1993–1999 scaled by a factor of 0.7 is used. The observations are assimilated asynchronously (Sakov et al., 2010) by using daily snap-shots of the ensemble SLA fields.

The SST data assimilated is sourced from OSTIA (OS-TIA Stark et al., 2007). The data set is available daily from
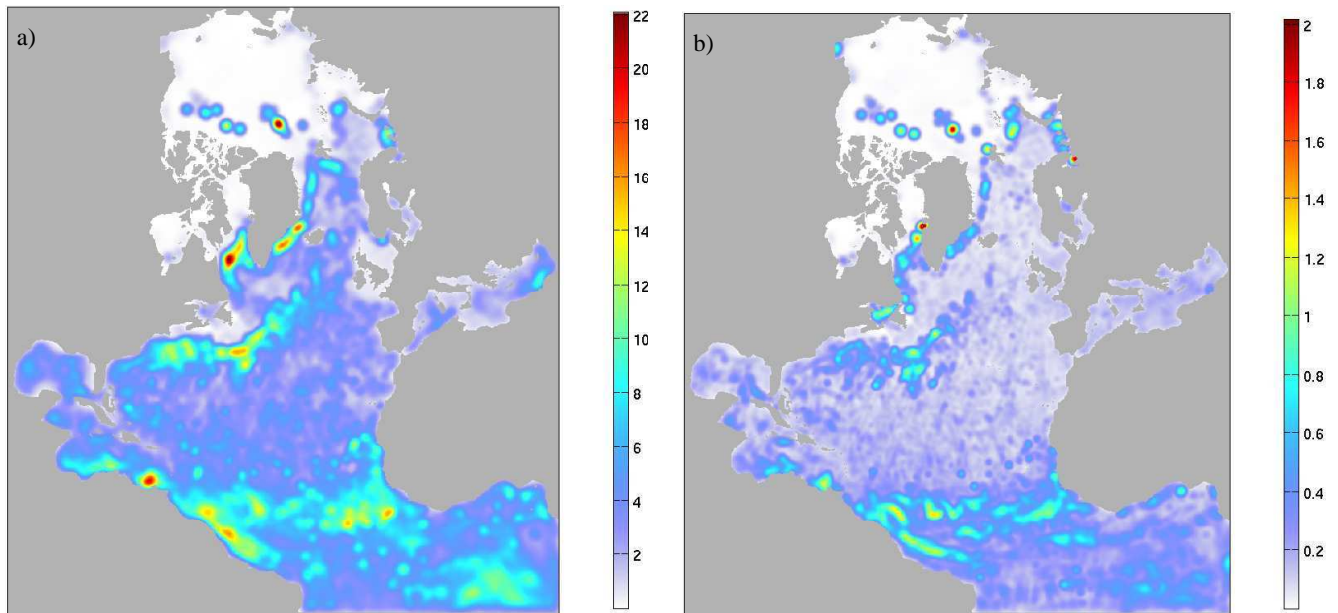
Fig. 3. Example of two-dimensional fields of the local DFS **(a)** and local SRF **(b)**; calculated in the course of the reanalysis for 23 April 2008.

1 April 2006 at horizontal resolution of approximately 6 km (though the spatial scales evident in OSTIA tend to be significantly coarser than 6 km), and is free of diurnal variation. It is a foundation SST product that combines data from infrared sensors (AVHRR and AATSR), microwave sensors (AMSR-E and TMI), and in-situ data from ships and surface drifting buoys. From the initial data set, the values retained include those that are within a realistic range (i.e. $\in [-1.9, 45]\,^\circ\mathrm{C}$) and away from the ice edge (mask provided with OSTIA data). The observation error estimated by the provider is purposely overestimated by a factor 2.5 to account for the representation error. Prior to 1 April 2006, TOPAZ4 uses version 2 of the Reynolds SST product (Reynolds and Smith, 1994) from the National Climatic Data Center (NCDC), which has a resolution of approximately 100 km.

The assimilated temperature (T) and salinity (S) profiles from Argo floats were downloaded from the Coriolis data centre at Ifremer. Unlike SLA data, in- situ temperature and salinity data are not assimilated asynchronously, and are instead assumed to correspond to the analysis time, even though they spanned the week preceding the analysis time. Profiles of T and S are checked for hydrostatic stability, and observations within each profile are superobed vertically to retain a maximum of one super-observation per layer, based on the layer structure of the first ensemble member. The forecast at each observation for each ensemble member is calculated by linearly interpolating between the adjacent layers of each member to the depth of the observation.

Beginning 18 April 2007, we assimilate in-situ T and S observations from hydrographic stations in the Arctic and Nordic Seas, using the same framework as for Argo observations. Additionally in-situ data are also assimilated from the

Nansen database that includes data from the International Polar Year (IPY), mainly the Ice-Tethered Profilers (ITP) which are currently the only observations available under ice. The scientific cruise data from the World Ocean Atlas (WOA05 Levitus et al., 2005, WOA09), ICES, IOPAS, IMR, AARI, Ocean Weather Station Mike, NABOS, NPI, North Pole Environment Observatory, the TRACTOR project, MMBI, LOGS are also assimilated after being manually quality checked (A. Korablev and A. Smirnov, personal communication, 2010). A total of 73 757 profiles are assimilated.

The map of locations of assimilated in-situ observations North of 50° N for the period from April 2007 to December 2009 is shown in Fig. 4.

The ICEC data is obtained from AMSR-E. It is computed with the ARTIST sea-ice concentration algorithm using AMSR-E 89 GHz brightness temperatures. The gridded data is available from 19 June 2002 at a resolution of 12.5 km. The spatial coverage is almost complete. TOPAZ4 assimilates the ICEC data on the day of each analysis. The observation error standard deviation is set to 10 % at the start of the reanalysis and is increased on 25 January 2006 to account for larger errors near the ice edge and to reduce overfitting at these locations. The error variance then becomes:

$$\sigma_{\mathrm{obs}}^2 = 0.01 + (0.5 - |0.5 - c|)^2,$$

where c is the observed ICEC. Prior to 19 June 2002 (during system spin-up), TOPAZ4 used the SSM/I data set at a resolution of 25 km. Brightness temperatures are sourced from the NSIDC and processed with the NORSEX algorithm, starting from 26 October 1978 with increasing resolution (Svendsen et al., 1983; Cavalieri et al., 1999).
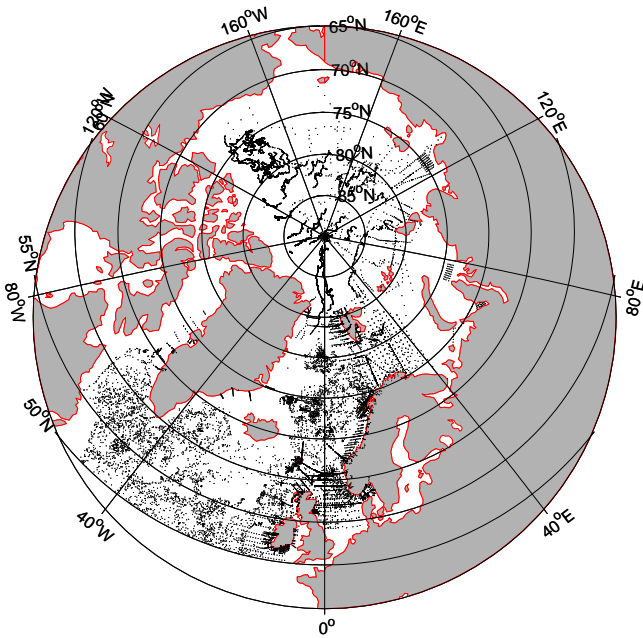
Fig. 4. The map of locations of assimilated in-situ observations north of 50N for the period from April 2007 to December 2009.

The sea-ice drift product is provided by CERSAT, Ifremer (Ezraty et al., 2006). The Lagrangian drift data is obtained at a resolution of 35 km by a pattern recognition algorithm from QuickSCAT, AMSR-E and SSM/I images. It is available from October to April inclusive and does not provide information close to the ice edge. The 3-day drift has been chosen as a compromise: long enough to average out some random errors in the composites that are computed over shorter periods and short enough to avoid severe loss of data near the coast that occurs in the composites computed over longer periods. The data is available from October 2002, but it is unavailable during summer due to loss of patterns where melting occurs. The provider accuracy estimate of 7 km/3 days is overestimated by a factor 2 to account for representation error.

Because the sea-ice drift data is Lagrangian, the corresponding observation operator is nonlinear. The model equivalent 3-days drift is computed for each ensemble member and each grid cell of the satellite data product. The initial positions are advected 3 days forward using model daily averaged ice velocities and a 2nd order Runge-Kutta method. The final displacements are computed on the observation grid.

4.3 Bias estimation

Bias estimation of SST and mean sea surface height (MSSH) was implemented in the reanalysis in February 2008. The following is a brief description of the bias estimation procedure.

1. The bias fields for each ensemble member are initialised to random spatially uniform values, with the standard deviation of the order of expected bias magnitude (the SST bias fields were initialised in the interval $[-4, 4]\,°C$; the MSSH bias fields – $[-0.6, 0.6]\,m$). There is no need to have spatial variations in the initial fields due to the use of localisation.

2. These fields are then augmented to the state vector.

3. During assimilation, the forecast observations for each ensemble member are offset by the value of the corresponding bias field. This involves SLA and SST observations, as well as in-situ temperature observations, which are offset up to the model depth of the mixed layer for a given ensemble member, with a smooth transition between offsetting by the full magnitude of the SST bias and no correction at about the mixed layer depth.

4. The bias fields are corrected due to their correlations with the forecast ensemble observations, which establish after a few assimilation cycles.

5. The bias fields remain constant during propagation, but their spread reduces after each assimilation cycle. Therefore, to avoid collapse of bias field ensembles, additional inflation is introduced (2 % per cycle for SLA, and 6 % for SST).

This bias estimation procedure is similar to that in the EnKF-Matlab package available from http://enkf.nersc.no/Code/EnKF-Matlab.

The difference in the magnitude of inflation for the SST and MSSH bias field is due to the fact that, as indicated by the innovation statistics, the SST bias has seasonal variability; while SLA is supposed to have substantial constant or interseasonal component.

Note that the bias correction doesn't explicitly *correct* the model bias, but rather diagnoses it. As a consequence, the best model estimate is the reanalysed state plus the diagnosed time-dependent bias. Also note that in TOPAZ4, the bias estimates are subtracted from the innovation, so that a well-behaved bias estimate reduces, on average, the innovation magnitude.

5 Results

5.1 Innovation statistics

The background innovation is a vector of differences between the observations and the model estimate of the observed quantities immediately before an assimilation is performed. Time series of the background innovation statistics, averaged over different regions (see Fig. 1 and Table 2), are shown for SLA (Fig. 5), SST (Fig. 6), and ICEC (Fig. 7).

Table 2. Boxes used for innovation statistics (see also Fig. 1).

Box ID	Box name	Min. lon.	Max. lon.	Min. lat.	Max. lat.
1	Nordic Seas	−30	20	63	80
2	Gulf Stream Extension	−50	−15	40	60
3	Gulf Stream	−80	−40	30	45
4	Tropical	−60	−15	0	20
5	Arctic	−180	180	70	90
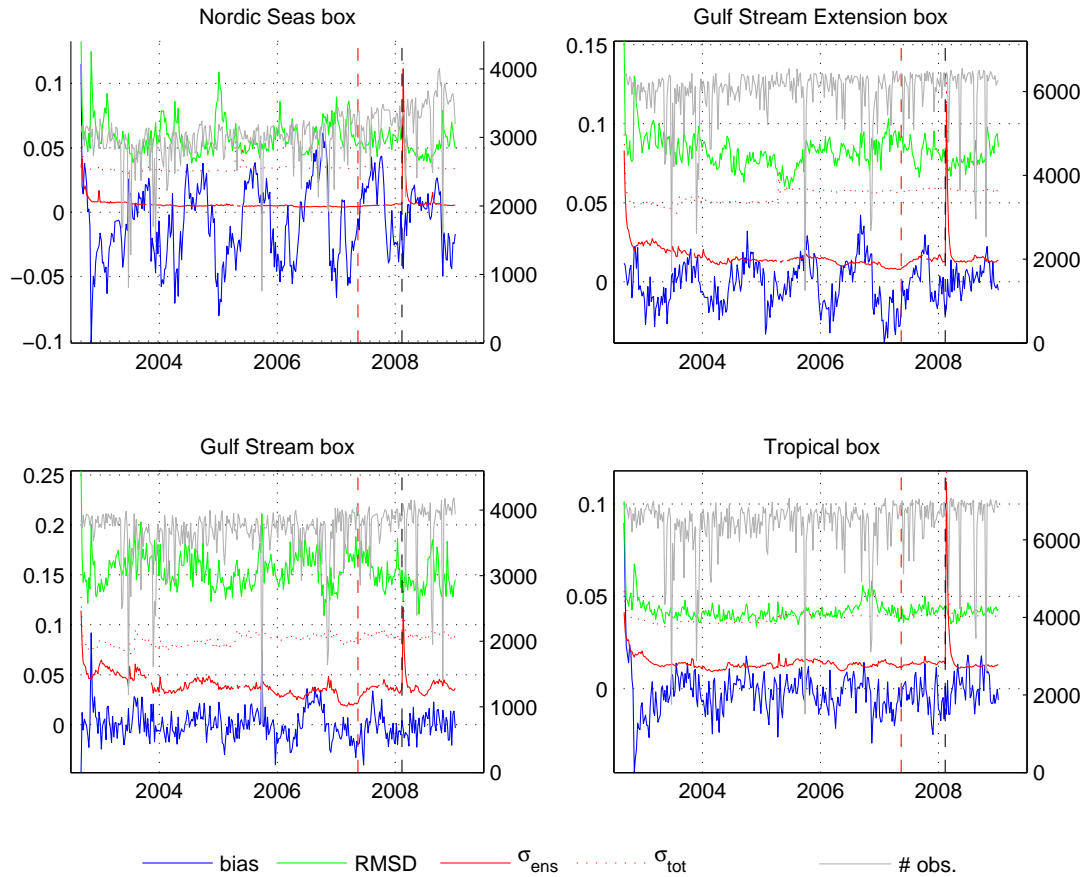
Fig. 5. Time series of regionally-averaged innovation statistics for satellite-derived SLA observations, including the bias (mean observed minus mean background; negative innovation bias corresponds to a warmer model), the RMSD between the observations and the model background field of the innovation, the ensemble spread σ_{ens}, and the estimated standard deviation of the innovation σ_{tot} (the quadrature sum of σ_{ens} and the assumed standard deviation of the observation errors). The boundaries to the regions are denoted in Fig. 1. The number of observations assimilated is also shown (grey line) with its corresponding axis on the right-hand-side of each panel. The Arctic region is not represented because there are no reliable remote SSH observations there.

In each case, time series are shown for the model bias (labelled bias); the root-mean-squared difference (RMSD) between the observations and the model background field (labelled RMSD); the standard deviation of ensemble anomalies (labelled σ_{ens}) that represents an estimate of the background error standard deviation; the estimated standard deviation of the innovation (labelled σ_{tot}) that is the quadrature sum of σ_{ens} and the assumed observation error standard devi-

ation σ_{obs}; and the number of observations to be assimilated (labelled # obs.).

Note that the RMSD and the bias are not independent (Oke et al., 2002). For different applications, different components of the RMSD might be more important. For example, the bias might be most informative for the assessment of sea ice extent and the freezing and melting of sea ice; while the correlation might be most informative for the assessment of eddies
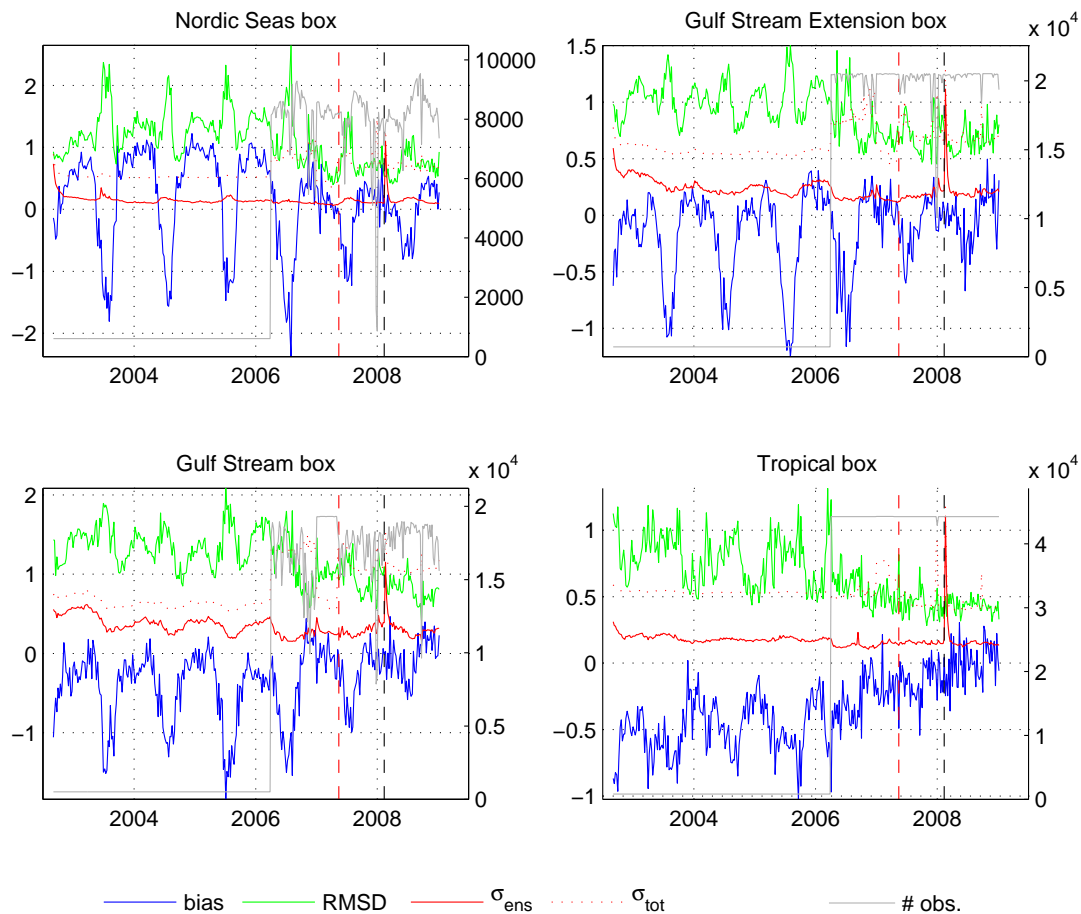
Fig. 6. Innovation statistics for SST (see description in caption to Fig. 5). The Arctic region is not represented because there are no remote SSH observations there.

and meanders, where the "shape" and phase of features in the ocean are important.

The time series of the innovation statistics for SLA (Fig. 5) show that the RMS of the innovations remained fairly constant throughout the reanalysis. These time series indicate that the RMS error for SLA is about 0.05 m in the Nordic Seas box; between 0.07 and 0.09 m in the Gulf Stream Extension box; between 0.13 and 0.18 m in the Gulf Stream box; and about 0.04 m in the Tropical box. We note a substantial seasonal bias in the Nordic Seas box, and to a lesser degree, in the Gulf Stream Extension box. The SLA innovation bias in the Nordic Seas box seems to exceed, on average, the estimated amplitude of seasonal steric height anomaly in the Nordic Seas (Siegismund et al., 2007, Fig. 5).

Generally, there is a good agreement between the estimated innovation standard deviation σ_{tot} and the measured RMSD for all presented fields. This demonstrates an internal consistency between the background and observation error variance and the innovations.

With regard to the innovation statistics for SST (Fig. 6), the RMSD of the innovations fluctuate throughout the period of the reanalysis, with a peak each year that corresponds

to a peak in the magnitude of the bias. This seasonal behaviour of the bias and RMSD is clearly seen in all boxes, except, perhaps, the Tropical box where the seasonality is weaker. The magnitude of the bias and the RMS are often comparable. This indicates that the RMSD between the reanalysed and observed SST is often dominated by the bias. In February 2006, the assimilated SST data was switched from Reynolds SST to OSTIA. The timing of this switch is evident in Fig. 6, when the number of observations increases significantly. The RMSD and bias decrease after this transition, indicating that the OSTIA SST is better suited to constraining the TOPAZ system. Prior to 2006, the RMS of the SST innovations in the Nordic Seas, Gulf Stream Extension, Gulf Stream and the the Tropical boxes is typically between 1.1–1.8 °C, 0.7–1.2 °C, 1–1.5 °C, and 0.6–1.0 °C, respectively. After OSTIA SST data started to be assimilated the RMSD of the SST innovations dropped to 0.5–0.8 °C, 0.5–1.0 °C (with the exception of the peak in summer 2006), 0.7–1.3 °C, and 0.4–0.5 °C in the Nordic Seas, Gulf Stream Extension, Gulf Stream, and Tropical boxes, respectively.

The bias correction, described in Sect. 3, was introduced in January 2008. This transition is denoted in Fig. 6 by the black
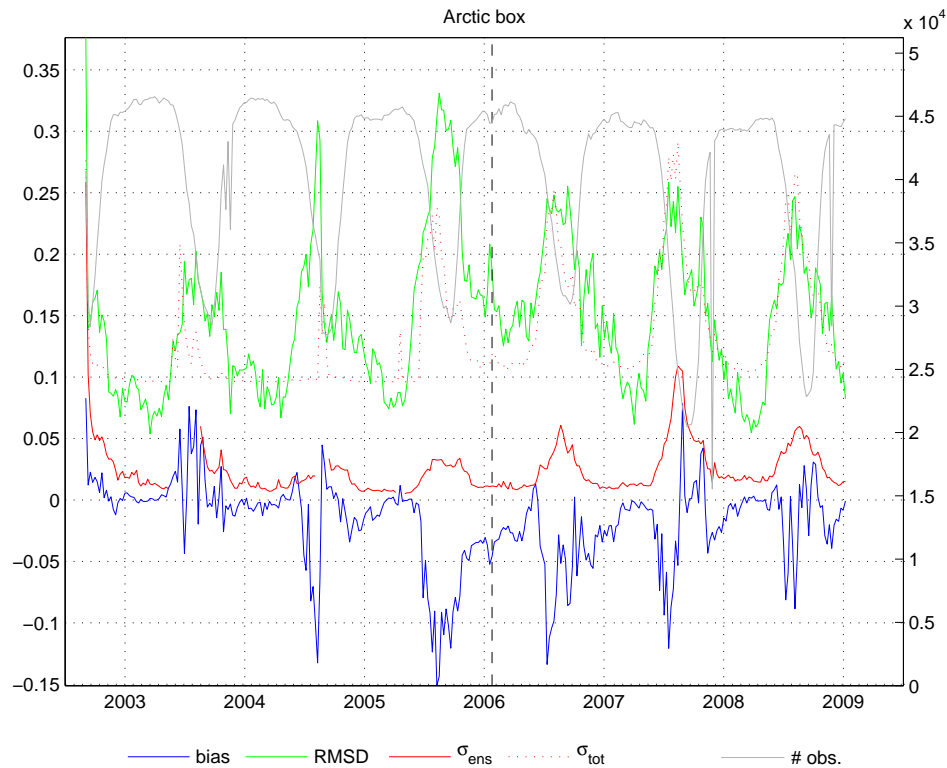
Fig. 7. Innovation statistics for ICEC (see description in caption to Fig. 5).

dashed vertical line. It is also marked by a sharp increase in the ensemble spread that includes the uncertainty in the bias. Although the bias estimation period is relatively short, the SST bias seems to decreases significantly after this point in the Gulf Stream and Tropical boxes, and decreases to some degree in the Nordic Seas and Gulf Stream Extension boxes; the RMS of the innovations also reduces after the bias is explicitly diagnosed and accounted for. Interestingly, the SST bias field does not show as much seasonal variability (not shown) as the bias of the SST innovations. This suggests that the seasonality of the SST bias that is evident in Fig. 6 may be related to the seasonal variations in the surface mixed layer depth. The surface mixed layer is generally deeper in winter. This is reflected in the ensemble-based background error covariance (not shown) that projects the SST innovations over a greater depth in winter. As a result, during winter, it appears that the assimilation of SST data better constrains the ocean model.

The vertical dashed red line in Fig. 6 denotes the time when the variance increasing factor of 2 for the update of the ensemble anomalies, described in Sect. 3.2, was introduced. It is expected to result in the increase of the ensemble spread and therefore the sensitivity of the DA system to observations. The impact on the ensemble spread is evident in Figs. 5 and 6, but any change in the sensitivity of the analysis system to individual observations is less clear. We suspect a parallel run without the variance increasing factor is needed to quantify this sensitivity.

The ensemble spread for SST remains relatively constant throughout the reanalysis for all domains considered here, indicating that the DEnKF showed no tendency towards ensemble collapse. It shows some seasonal fluctuations in each box except the Tropical box, with greater spread in winter and less in summer.

For an optimal data assimilation system, σ_{tot} should match the RMS of the innovations. Clearly, for SST prior to the switch to OSTIA SST, σ_{tot} was too small by about 50 % of the RMS, but was approximately correct after the switch to OSTIA. This indicates that either the ensemble spread, σ_{ens}, was too small before the switch to OSTIA, or the assumed observation errors for Reynolds SST were too small. We suspect that the latter is true. The consistency between the actual innovation, given by the RMSD, and the estimated innovation, given by σ_{tot}, demonstrates a consistency between the assumed and computed background and observation errors, and the actual errors of the background fields in the reanalysis.

The time series of the innovation statistics for ICEC is shown in Fig. 7. The most notable feature in the time series of RMSD is the peaks each summer. This occurs because summer is the period when sea ice variability is highest. At the start of summer, sea ice melts and at the end of summer it begins to freeze. The timing of this melting and freezing each
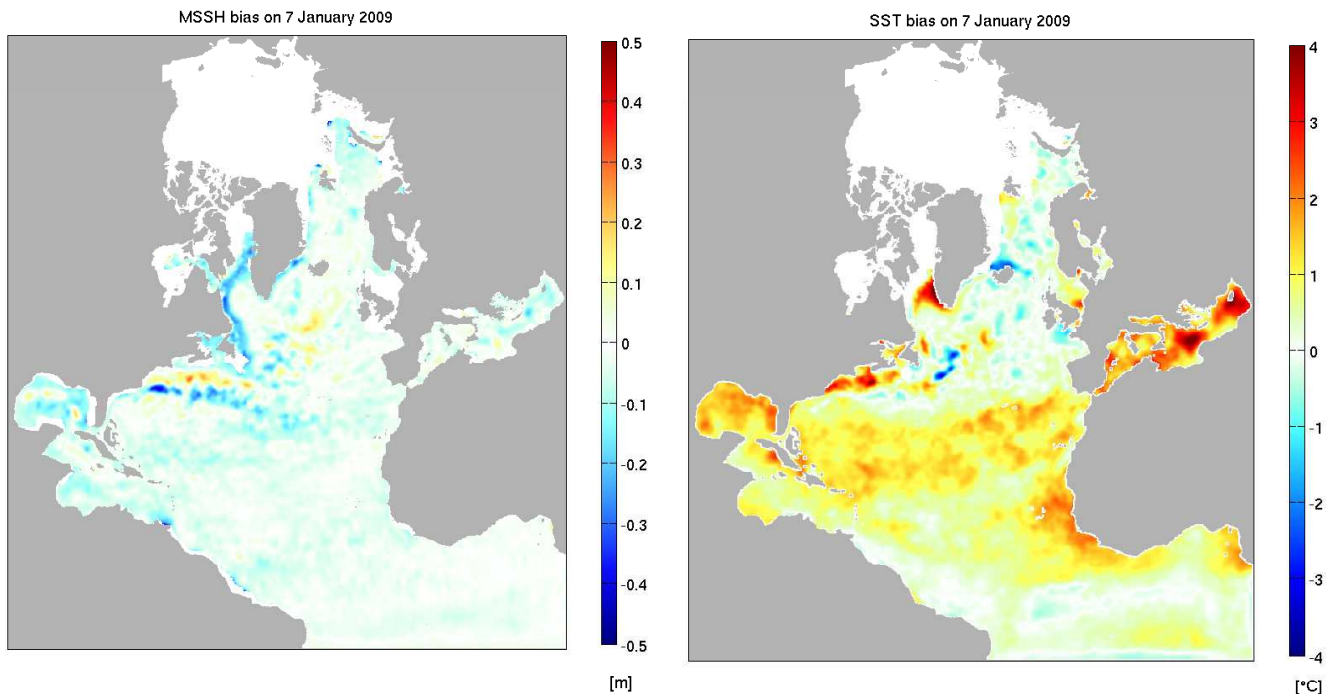
MSSH bias on 7 January 2009

SST bias on 7 January 2009

[m]

[°C]

Fig. 8. Estimated MSSH and SST bias fields at the end of the reanalysis (after 10 months of estimation). Regions with no observations available at that time are masked to 0. Positive bias corresponds to a higher model MSSH/SST compared to observations.

summer can be seen in Fig. 7 when the number of observations assimilated substantially decreases and then increases again, reflecting the ice extent. Note the strong correlation between the RMSD and the bias. This indicates that a significant portion of the RMSD is attributed to the bias.

The vertical dashed black line marks the time when a number of changes have been introduced into the system after observing some excessive increments in salinity in the course of assimilating ICEC. These changes include the introduction of adaptive observation pre-screening (Sect. 4.2), increasing the perturbations of model forcing to affecting the position of the ice edge (Sect. 3.3), and relaxation of the assumed observation error variance (Sect. 4.2). These changes seem to improve the performance of the system in regard to the ICEC. For example, there is an increasing trend in the RMSD prior to the change, which is then reversed.

The time series of ensemble spread shows a peak each summer that is in phase with the peak in RMSD. Moreover, the time series of the estimated standard deviation of the innovation σ_{tot} is remarkably well-aligned with the RMSD.

This demonstrates an internal consistency between the actual errors, quantified by the RMSD, and the assumed and modelled estimates of the errors, from the estimated observation errors and the ensemble-based estimate of the background field errors. This is a very encouraging result, because it demonstrates that the time-varying estimate of the background field errors from the ensemble can be used to quantify the error in the system in advance. This internal con-

sistency and functionality is highly desirable for every data assimilation system – but it is rarely achieved in practice.

5.2   Bias estimates

The estimated bias fields for MSSH and SST at the end of reanalysis are presented in Fig. 8. An assessment of the bias estimate for MSSH is provided in Fig. 10, where we compare the MSSH derived from TOPAZ before the bias correction is introduced (from a free run of the model), after the bias is introduced (from the reanalysis), and the observations-only MDT from CNES-CLS09 (Rio et al., 2009), not assimilated. The revised MSSH after the bias is introduced is constructed by adding the time-mean estimate of the SSH bias with the MSSH from the free model run. Several aspects of the revised MSSH are in better agreement with CNES-CLS09 MDT than the MSSH from the free model run. For example, the Gulf Stream at Cape Hatteras shoots too far north in the free model run, as one expects from a model of this resolution, is shifted southwards and is more confined in the revised MSSH. The improvement is visible in the meridional section at 60° W in Fig. 9, where the MSSH drop south of 40° N is sharper after bias estimation and SSH peak on the southern side of the Gulf Stream is also reproduced. The correlation between the model and observations increases from 0.71 to 0.74. We also note that the extent of the Sub-polar Gyre in the Labrador Sea is reduced in the revised MSSH, in agreement with the CNES-CLS09 MDT, and the permanent anticyclonic eddy at the southern tip of the Sub-polar
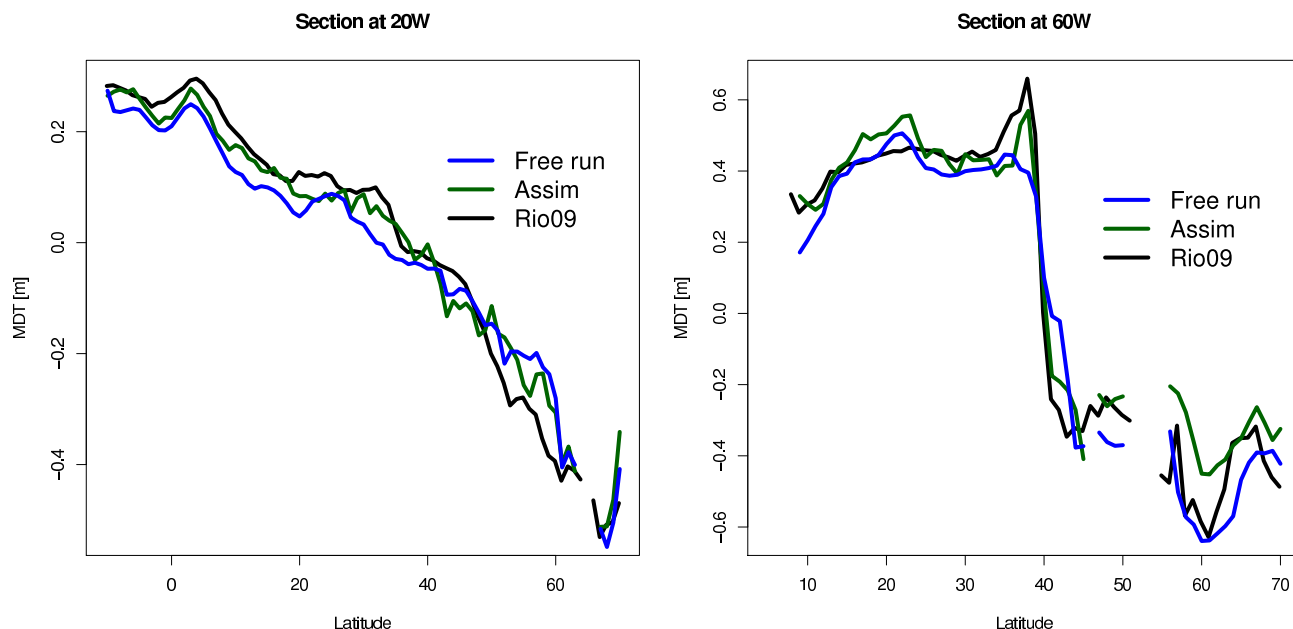
Fig. 9. Sections of MDT from Rio09 (black), HYCOM free run (blue), and estimated with data assimilation (green). An offset of 15 cm has been removed from the Rio09 data.
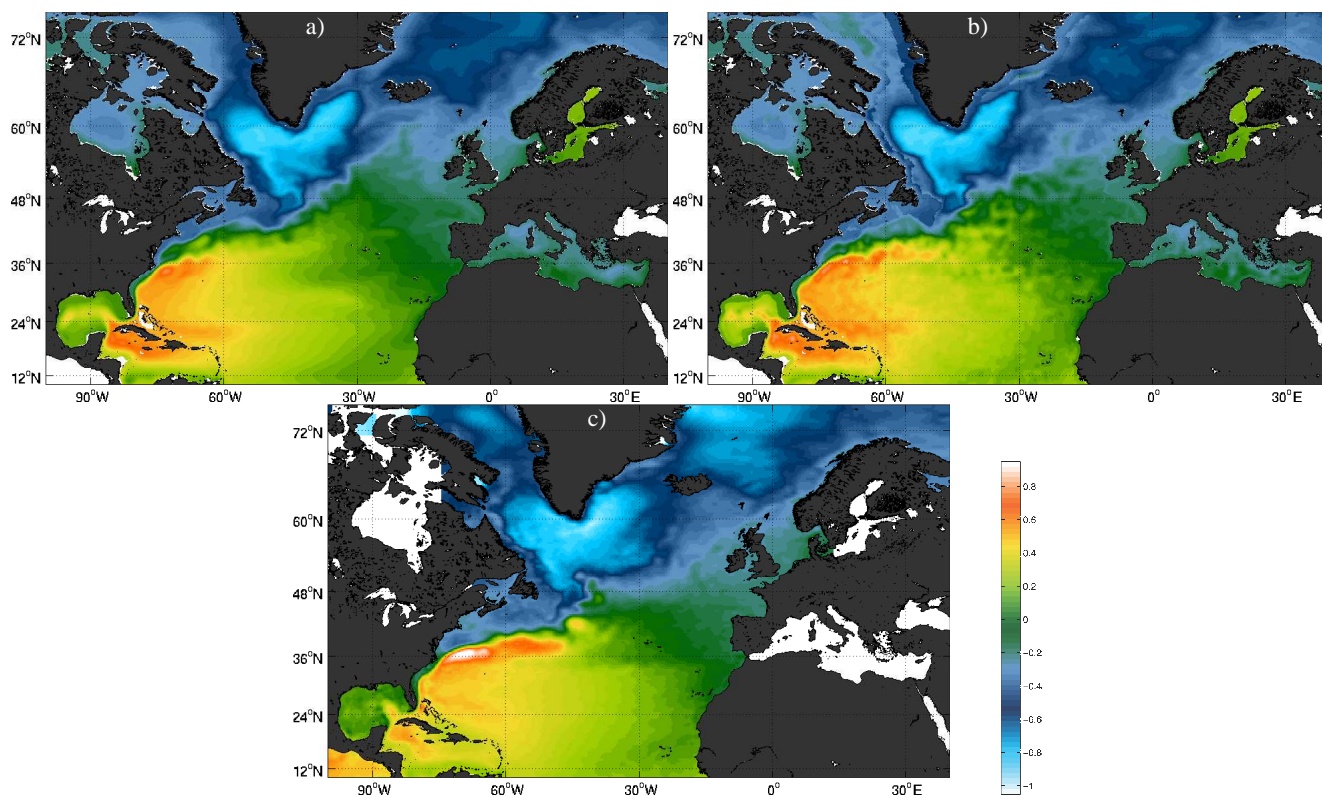

Fig. 10. (a) TOPAZ4 MSSH before bias correction; **(b)** TOPAZ4 MSSH after bias correction; **(c)** MDT from CNES-CLS09.

Gyre that is evident in CNES-CLS09 MDT is also evident in the revised MSSH, but is not clear in the original MSSH. Fi-

nally, the two branches of NAC inflow into the Nordic Seas are re-equilibrated – the Icelandic branch of the NAC is too

17 January 2007

18 April 2007

18 July 2007

17 October 2007

SSH [m]
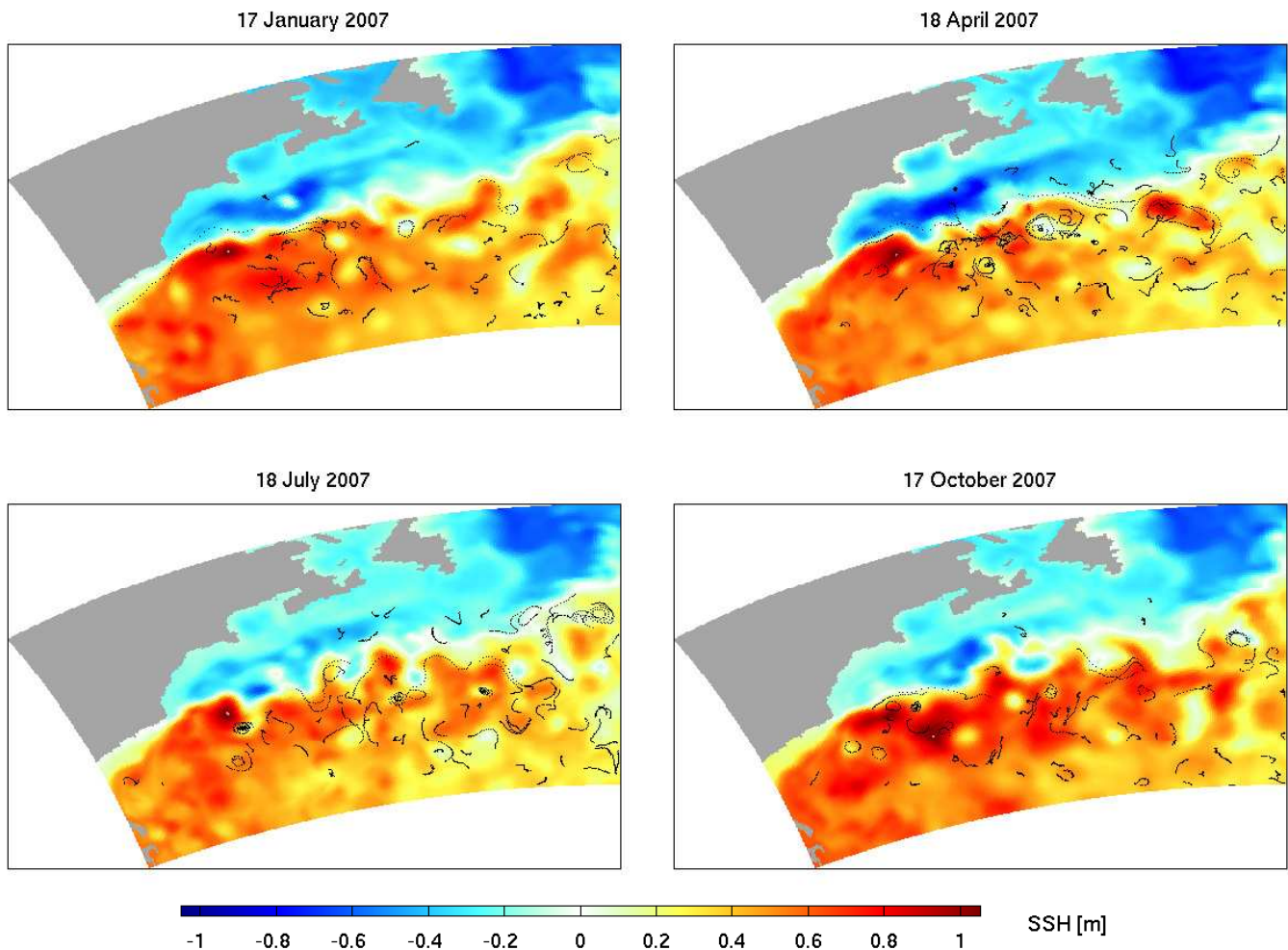
Fig. 11. Drifter trajectories in the Gulf Stream box (dots) versus the analysis SSH. The drifter positions are plotted at 6 h time step within ±4 days from the day of the analysis (given at the top of each panel).

strong in the original MSSH. This is also illustrated in the meridional section at 20° W in Fig. 9: the downward slope between 40° N and 60° N is steeper after bias estimation, in better agreement with the observations. Here again, the correlation increases from 0.86 to 0.92.

An attractive aspect of the online bias estimation is that it requires no hand-tuning of the MSSH. The joint assimilation of satellite observations and in-situ Argo temperature and salinity profiles (mostly in-situ data) are solely responsible for the corrections to the MSSH.

The SST bias field (Fig. 8) shows several regions of spatially coherent positive bias, including regions in the Gulf of Mexico and the Caribbean Sea, the southern part of the sub-Tropical Gyre and parts of the Mediterranean Sea. In these areas the model is warmer, indicating either that the net surface heat flux is too high or that the modelled surface mixed layer is too shallow – so that not enough sub-surface water is entrained into the surface layers. There are also several regions along the path of the Gulf Stream Extension where

the SST bias is large and negative. We suspect that this is an indication that the path of the Gulf Stream is too far to the south.

5.3 Comparison with drifting buoys

A series of SSH maps for different seasons is presented in Fig. 11 with drifter trajectories overlaid. In each map, we show the position of all available drifters, obtained from http://www.meds-sdmm.dfo-mpo.gc.ca/isdm-gdsi/drib-bder/svp-vcs/index-eng.asp on 3 March 2011. Each map in Fig. 11 shows daily averaged SSH and 6-hourly drifter positions for a 9-day window centred on the model time. The purpose of this analysis is to provide an independent qualitative assessment of the mesoscale variability in the reanalysis. Since the ocean circulation is dominated by geostrophy, we expect the drifters to flow along paths of constant SSH, and we hope to see good correspondence between the drifter paths and the mesoscale features in SSH. In most cases, we find that there is good correspondence
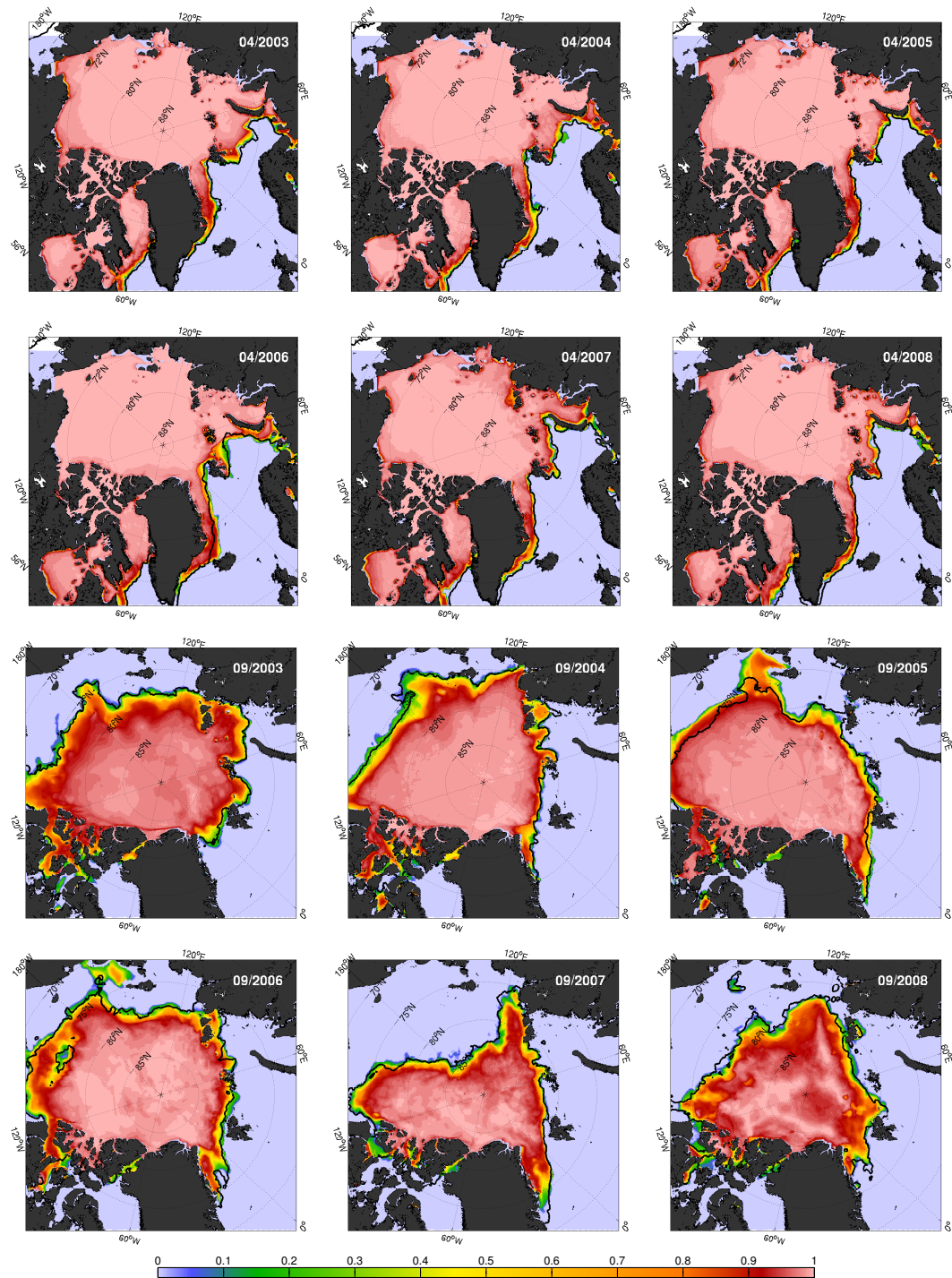
Fig. 12. Monthly average ICEC reanalysis fields for for April (two top rows) and September (two bottom rows). The thick black line shows the 15 % concentration contour derived from the monthly average observation based ICEC from AMSR.

between the SSH fields in the reanalysis and the independent observations of drifter paths. In many cases, even the details of the drifter paths are well captured by the reanalysis.

The good comparisons between drifter paths and modelled SSH demonstrates that the TOPAZ system produces realis-

tic variability in the North Atlantic Ocean. The good performance of the TOPAZ reanalysis in the North Atlantic confirms that the model is "sufficiently eddy permitting" to provide a realistic representation of the mesoscale variability in the Gulf Stream region. This is very encouraging, because
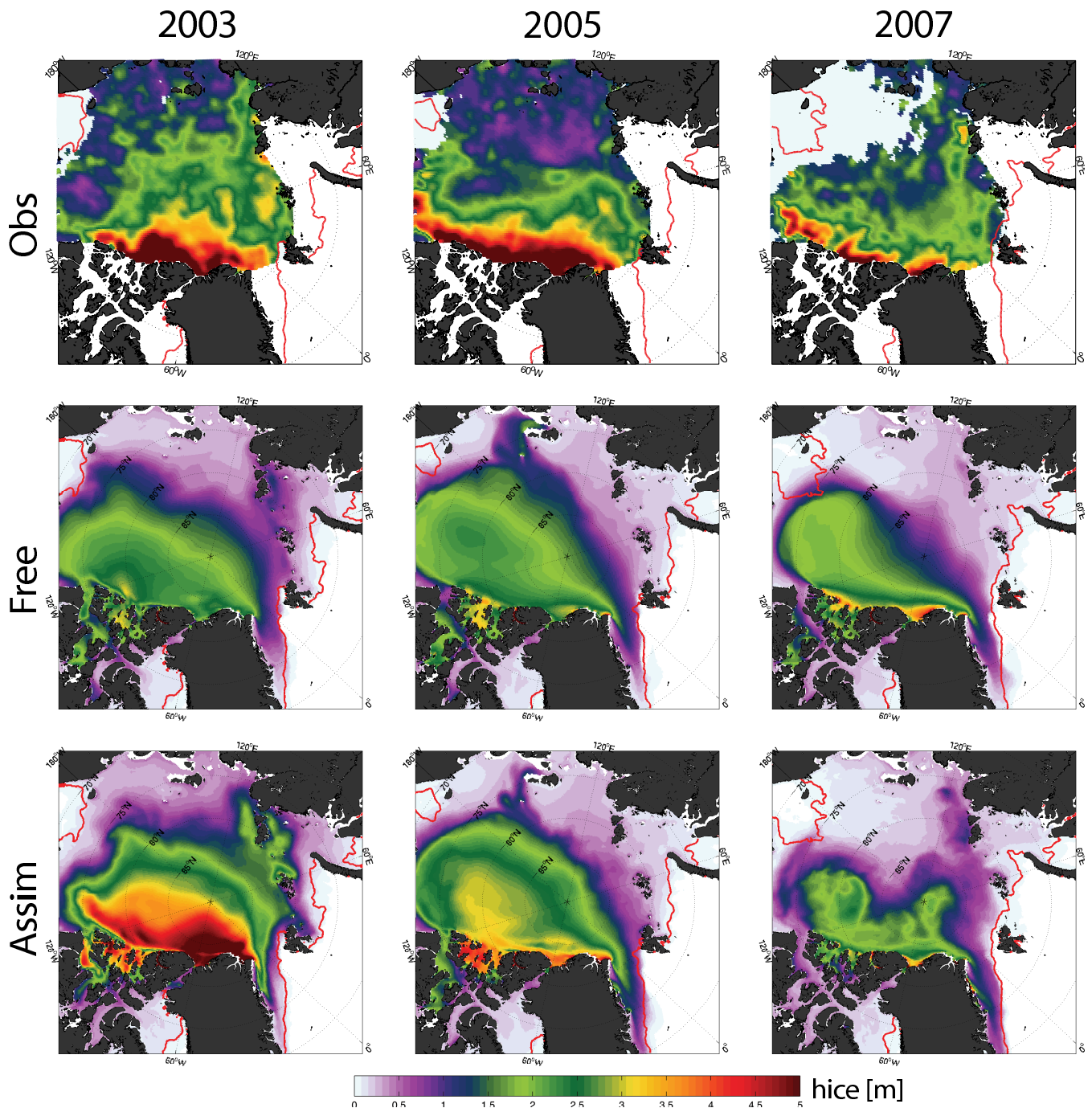
Fig. 13. Average fields for the ice thickness for October–November; for observations from ICESat (Kwok and Rothrock, 2009), free run and reanalysis. The red line shows the contour of 15 % ICEC from AMSR data.

the focus of the TOPAZ developments is the Arctic Ocean, not the North Atlantic Ocean.

We note that a similar comparison between drifter paths and the free running model without data assimilation shows no correspondence between individual mesoscale features in the model and observations (not shown). This is what we expect, and is a consequence of the chaotic nature of mesoscale

variability. Individual eddies and meanders spawn from instabilities that are difficult to predict and model explicitly. Although the model may be capable of reproducing eddies and meanders with the right variability, and in the right locations, without data assimilation it is unable to predict precisely when and where an instability will occur.
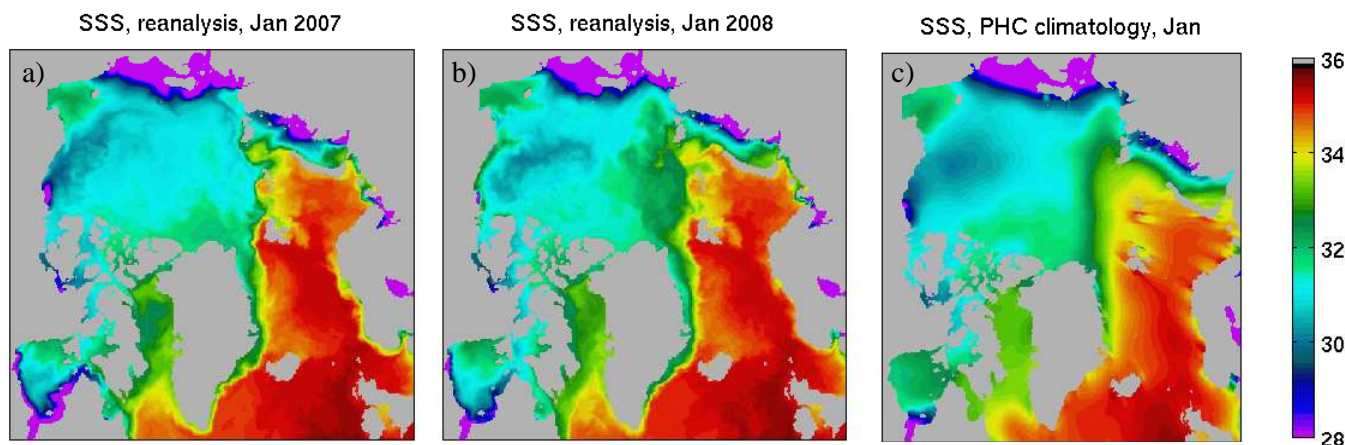
Fig. 14. Mean monthly SSS: **(a)** for January 2007 by TOPAZ4; **(b)** January 2008 by TOPAZ4; **(c)** for January from PHC climatology.
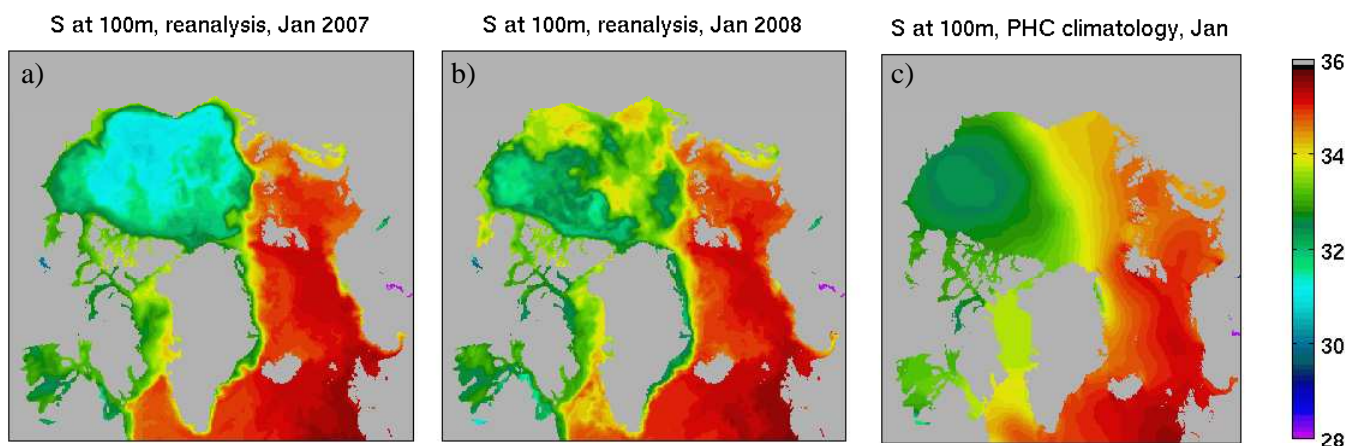

Fig. 15. Mean monthly salinity at 100 m: **(a)** for January 2007 by TOPAZ4; for January 2008 by TOPAZ4; **(c)** for January from PHC climatology.

5.4 Evaluation of ice fields

To demonstrate the quality of ICEC field in the reanalysis, we show in Fig. 12 comparisons between the monthly average reanalysed ICEC and monthly average ice edge contour drawn at 15 % of ICEC based on the AMSR data. The data are presented for April and September, which represent the months with maximal and minimal total sea ice extent.

The correspondence of the reanalysed and observed sea ice extents is generally quite good, except September of 2005 and 2006, when the model produced too much sea ice. These periods can also be in the RMSD of the innovation of ICEC in Fig. 7; however, we note that the RMSD seem to peak somewhat earlier in the year. We note that the sea ice extent in TOPAZ is particularly good off eastern Greenland and off Spitsbergen (Svalbard). These regions are key regions of interest for many applications. The Fram Strait is the only deep passage between the Arctic and the and the rest of the Worlds Oceans. The crossing of the North Atlantic and Arctic waters

needs to be monitored as well as the export of sea ice from the central Arctic into the Greenland Seas, which depletes the ice pack (Kwok, 2009).

The comparisons of early Fall ice thickness in Fig. 13 show that the data assimilation has done limited change to the overall distribution of ice in the Arctic, in line with Lisæter et al. (2003) who found that the assimilation of ice concentrations mostly impacted the position of the ice edge, but not so much the ice volume. The ice is too thin in areas of thick ice and inversely, too thin in areas of thick ice, which is a common feature in models that use a viscous rheology (Johnson et al., 2012). The assimilation has indeed slightly thickened the ice there, which – by elimination – is likely to be the effect of assimilating ice drift. The ice is also thickened to the North of Franz Joseph Land and Siberian Islands, in better agreement with the ICESAT data, which reflects the better position of the ice edge during the ice minimum.

The comparison of the ice drift from TOPAZ with that from IABP buoys and the Tara expedition (not shown)

reveals that the model ice drift is generally slightly too fast, by 3 km day^{-1} for slow drift as much as for fast drift, which is a known deficiency of the EVP type of model: Girard et al. (2009) reported an even larger bias of 6 to 7 km day^{-1}. The too fast ice drift is advecting too much ice into the Beaufort Sea and is consistent with the ice pack being spread out, as mentioned above.

5.5   Evaluation of salinity and temperature

Below we will mainly concentrate on the evaluation of salinity, which is the most important tracer for circulation in the Arctic; but we will also provide some temperature comparisons with mooring data.

A comparison of SSS from the TOPAZ reanalysis, from the GDEM climatology (Teague et al., 1990), and from a free run of the model (not shown) indicates that these SSS fields are very similar in the North Atlantic. By contrast, there is a significant improvement in the SSS of the reanalysis in the Arctic compared to that of the free running model.

Figures 14 and 15 show the monthly mean SSS and the monthly mean salinity at 100 m depth (S100) for the reanalysis during January 2007, before in-situ observations in the Arctic are assimilated, and during January 2008, after in-situ observations in the Arctic are assimilated. For comparison, we also show an estimate of SSS climatology from PHC (Steele et al., 2001).

The SSS and S100 fields in January 2007, before in-situ observations in the Arctic are assimilated, show an unrealistically large and misplaced Beaufort Gyre, with too low salinity. The salinity of the free run is very similar to that of the reanalysis in January 2007 (not shown). In spite of this model deficiency, the intensity and location of the Beaufort Gyre are corrected efficiently by assimilation of the profiles. We interpret this improved performance in 2008 as an indication that the assimilation of in-situ observations in the Arctic is beneficial, and has had a measurable positive impact on the reanalysis (however, see Sect. 5.8 in regard to the patchiness observed in the middle panels of Figs. 14 and 15).

In particular, the assimilation of ITP profiles appears to be critical for constraining the central Arctic temperature and salinity structures, even though the number of ITP profiles was limited. Indeed, the total DFS and SRF, presented in Fig. 3, show that the efficiency of these profiles under ice is very high compared to other observations in the high latitudes, confirming that these data had a very significant impact on the reanalysis.

The temperature and salinity profiles in the Arctic are assessed against the NABOS/CABOS moorings in Fig. 16. The moorings were active before the assimilation of ITP data but not assimilated. The temperature profiles in the Laptev Sea reveal insufficient transport or excessive diffusion of warm Atlantic Water. Although transport estimate in the Fram Strait compares well with observations(see Sect. 5.7), the core of Atlantic Water is too weak and too diffuse (see Sect. 5.6). This excessive diffusion may result from the artificial thickness diffusion used for model stability or from our parametrisation of diapycnal mixing that does not account for the attenuation of internal waves below sea ice (Morison et al., 1985; Nguyen et al., 2009).

For the Canadian mooring the comparison with observations for both the reanalysis and the free run is quite poor. Note, however, that historically TOPAZ has been calibrated for the North Atlantic and the adjacent Arctic sector rather than for the Canadian basin. Both simulations show a too shallow and too cold Pacific Water, which is likely to be a direct consequence from disregarding seasonal variability in the Bering Strait inflow. The reanalysis does not show the Atlantic layer presented in observations, and in this instance, the free running model is closer to observations. However, in view of the relatively patchy horizontal fields (not shown), we suspect the deterioration of the reanalysis to be an isolated case rather than reflecting a general tendency.

5.6   Comparison with hydrographic sections

The Fram Strait is the main oceanic gateways between the Atlantic and the Arctic Ocean and is thus the most important region for the exchange of Atlantic and Polar water masses. Since 1997 oceanic fluxes through Fram Strait have been monitored by an array of moorings deployed between 6°30′ W and 8°40′ E at the latitude 78°50′ N (Schauer et al., 2008; Beszczynska-Möller et al., 2011). This data-set is not assimilated during the pilot reanalysis and can be thus considered as independent. Several water masses are present in the Fram Strait. Near the surface on the eastern side, there are several branches of the warm and saline Atlantic Water (inflow and recirculation). On the western side the East Greenland Polar front englobe the fresh and cold Polar Water. Between 800 m and 1200 m, one can find the Arctic Intermediate Water and the Upper Polar Deep Water with a temperature close to 0 °C. Bellow, the Nordic Sea Deep Water and the Arctic Ocean Deep Water are present.

Figure 17 compares temperature from the free and assimilative runs to the data in the winter and summer 2007. The improvements from data assimilation are numerous. The Atlantic Water in the free run is too cold, too deep and diffuse. This is much improved in the reanalysis even if the multiple cores are not clearly represented and the core of Atlantic Water is still too deep and slightly too diffuse. The Polar Water is also too deep in the free run. In the reanalysis the water is located at a reasonable depth but extends too far to the east. Both the free run and the reanalysis misrepresent the deep water. The differences in the intermediate and deep water are small, but the stratification is better pronounced in the reanalysis and the deep water is slightly colder. It appears that the influence of data assimilation at depths is minor.

It is worth mentioning that the comparison in the Fram Strait is affected by the initialisation problem described in Sect. 5.8. In a normal free run (initialised from a long
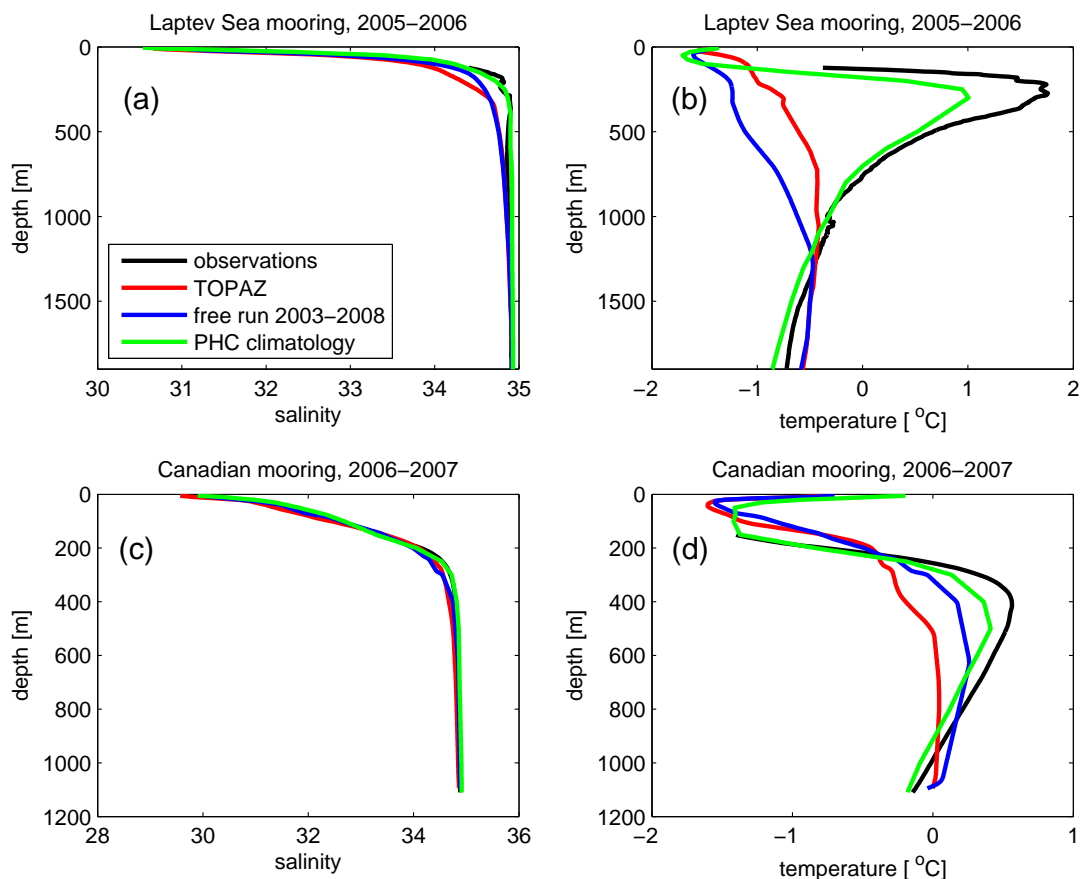
Fig. 16. Salinity **(a, c)** and temperature **(b, d)** profiles for the Canadian mooring C1F (71.50° N, 131.47° W) and Laptev Sea mooring M1C (78.43° N, 125.61° E), compared with PHC climatology, free model run and reanalysis; all data is averaged over the observation period (C1F: 12 September 2006–28 August 2007; M1C: 15 September 2004–15 September 2005).

spin-up), the water masses are in better agreements to observations than in the free run started the initialisation problem.

5.7 Volume transport estimates

Time series of 3-monthly averaged volume transports through the Svinøy section and Barents Sea Opening (denoted in Fig. 1), from the reanalysis and from independent observations, is presented in Fig. 18. The Svinøy section is a key location for measuring the Atlantic inflow to the Norwegian Sea, due to the topographic steering of the Norwegian Atlantic Slope Current (NwASC) and its vertical structure. Skagseth et al. (2008) estimate the volume flux from one single mooring in the core of the flow. After passing through the Svinøy section, the NwASC flows northwards into the Arctic and splits in two branches between Norway and the Spitsbergen and between the Barents Sea Opening (BSO) and the West Spitsbergen Current (WSC). Another array of moored current measurements in the BSO monitors the fluxes between Norway and Bear Island (Ingvaldsen et al., 2004). The associated uncertainty estimates are not provided in either case, but differences should be expected between the punc-

tual current measurements and the section-averaged volume fluxes, even after low pass filtering. The velocity measurements used to generate the observational estimates of the volume transport in Fig. 18 were not assimilated in the reanalysis.

In the Svinøy section, the transport estimate from the free run is too low (3.5 Sv) compare to observation (4.7 Sv) and the one from the reanalysis is too high (6.1 Sv). The free run transport is too low until 2005, but then adjusts to a level that is comparable to the observation while the reanalysis transport remains offset during the whole integration. The variability is relatively well captured by the model but the reanalysis correlates better with the observations, with the correlation coefficient increasing from 0.7 to 0.8. Both model runs represent reasonably well the seasonal variably but the interannual variability of the volume transports is better reproduced by the reanalysis with an increasing trend until 2006, followed by a decreasing trend.

In the BSO, the interannual variability is missing, and the model does not represents the very high maximum in 2006 nor the decreasing trend, and the correlation is poor (0.42 for the reanalysis and 0.40 for the free run). We attribute
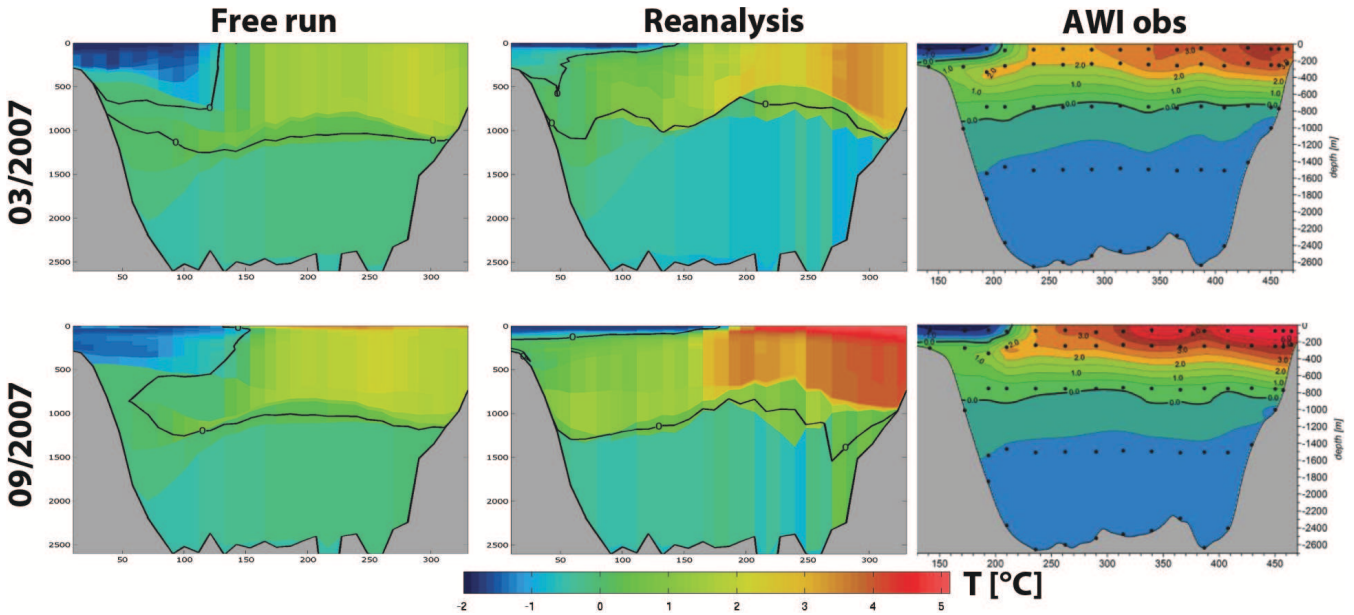
Fig. 17. Temperature in the Fram Strait section from the free run, reanalysis and observations.
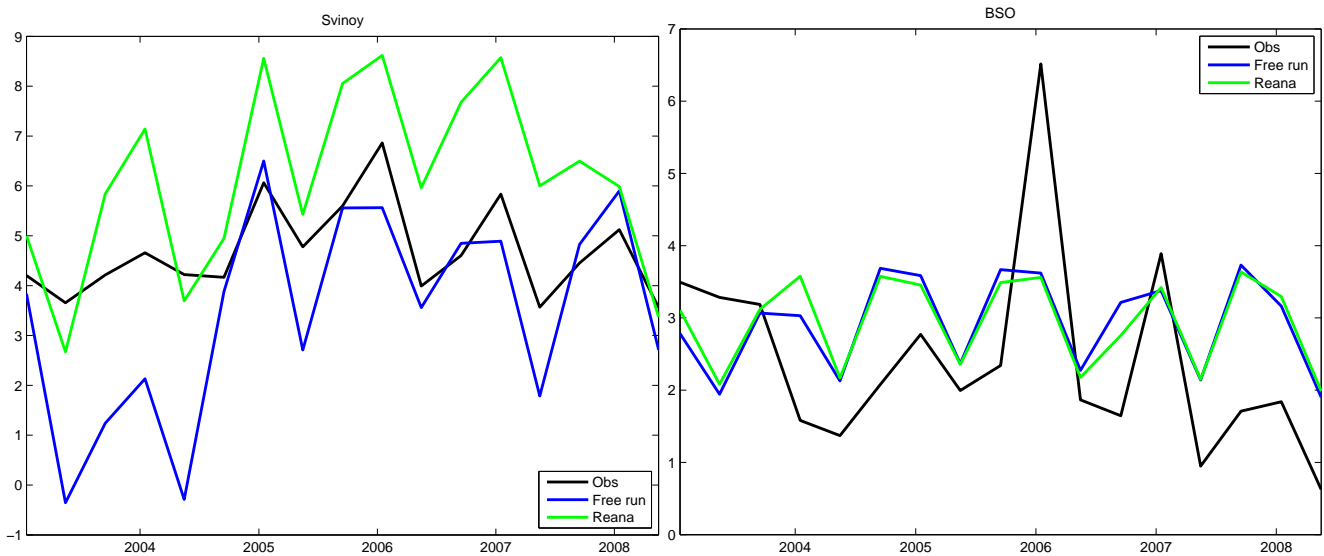

Fig. 18. Comparison of 4-monthly average transport through the Svinøy section and Barents Sea Opening section from observations, free model run and TOPAZ reanalysis.

this difference to insufficient resolution in the surface forcing fields (from ERA-interim) that does not accurately represent winter storms and polar lows. The transport is overestimated in both the free run and the reanalysis (with 2.9 Sv instead of 2.2 Sv from observations). Still, the free and assimilated run are very close to each other and reasonably close to the observations with respect to other model products of higher resolution (Gammelsrød et al., 2009).

Finally, the transport in the Fram Strait is analysed against the estimate from Mauritzen et al. (2011) computed between 2002 and 2008. The net Southward transport is respectively

2.3 Sv and 2.2 Sv for the free run and reanalysis, well in line with the observed transport of 2.08 Sv.

Overall, the magnitude of the volume transport in the reanalysis in the Svinøy section, BSO and Fram Strait are in good agreement with the observed estimates. This indicates that the partitioning of the current between the NwASC, the BSO, and WSC is well reproduced in the reanalysis.

There is no temporal trend evident in the volume transport estimates in Fig. 18. This indicates that the modifications to the details of the assimilation that were introduced in

the course of the pilot reanalysis did not abruptly impact the reanalysed circulation in the Nordic Seas.

The coverage of the observation network also changes over time, including the addition of Argo profiles in the Nordic Seas in early 2007. We did not find that this change results in any significant change of the circulation, although the assimilation of Argo profiles may have improved the fit of the volume transport in the Svinøy section in 2008 compared to the previous years (Fig. 18), but a longer integration is needed to be sure of this result.

5.8 Known problems

After completing the reanalysis, a problem was identified in the superobing code for in-situ temperature and salinity observations that affected a small proportion of in-situ observations for the Arctic and Nordic Seas during 2007 and 2008. We believe that this issue had no major impact on the reanalysed fields due to the small amount of erroneous observations (less than 1 %) and due to the adaptive observation pre-screening procedure (Sect. 3.2); however, we found that this error causes some instances of patchiness in the reanalysed fields in the Arctic.

A hardware (Input/Output) problem has been identified that has affected the system in November 2002, before the start of the reanalysis. The most obvious impact was an anomalously wide Beaufort Gyre containing too much fresh water. In order to assess only the impact of assimilation, the free run has been initiated after the November 2002 problem.

In the course of the reanalysis, and with the assimilation of the ITP profiles, the Beaufort Gyre was restored to a reasonable size, though several imperfections remain visible, far from the ITPs locations.

Some model parametrisations were also found inappropriate. A constant inflow in the Bering Strait leads to biased fresh water and heat fluxes (Ness et al., 2010). The inflow of Atlantic Water in the Fram Strait is diffuse supposedly because the diapycnal mixing and layer thickness diffusion were not calibrated specifically for the Arctic.

6 Conclusions

The purpose of this paper is to provide a description and evaluation of TOPAZ4, the latest version of TOPAZ – a coupled ocean-sea ice data assimilation system for the North Atlantic Ocean and the Arctic. TOPAZ is the only operational, large-scale ocean data assimilation system that uses the EnKF. The version of the EnKF used in TOPAZ4 is the DEnKF (Sakov and Oke, 2008a). We show that the state-dependence of the background error covariance is particularly important for a coupled ocean-sea ice system because of the strong non-stationarity and anisotropy of correlations between physical fields across the ice edge. This sets the current application apart from many other short-range ocean forecast systems

that are developed for open ocean forecasting, and not coupled ocean-sea ice forecasting.

We provide an evaluation of TOPAZ4 through a pilot MyOcean reanalysis that spans the period 2003–2008. We demonstrate that TOPAZ4 produces a realistic estimate of the ocean circulation in the North Atlantic and the sea ice variability in the Arctic. One of the potential strengths of any EnKF-based data assimilation system is that it predicts and evolves the system's state error covariance implicitly in the ensemble, as well as the system's state. Thus, it provides an estimate of the system errors in real time. We evaluate this aspect of the TOPAZ4 system by analysing the innovation statistics of the reanalysis. We find that the ensemble-based estimate of the background error variance for SST and SSH remain fairly constant throughout the reanalysis and that, after accounting for the system's bias, this is consistent with the misfits between the model fields and the assimilated observations. We also find that the variance of the ensemble – the system's online "prediction" of the background error variance – for ICEC is well correlated with the misfits between the model and observations. This result demonstrates that the ensemble statistics could be reliably used to obtain state-dependent error estimates for the system – a feature that is unique to ensemble-based data assimilation systems.

During the course of the reanalysis, we introduce various modifications to the assimilation configuration, and to the observations assimilated. For example, we switch the source of SST data that is assimilated, and we introduce an explicit online bias estimation. We recognise that this approach is not systematic, and leaves some uncertainty about the specific impact of each of these changes. However, the cost of performing an independent reanalysis to evaluate the impact of each and every modification is prohibitively expensive, and is probably not warranted. Despite this, we can infer the impact of the modifications by analysing the changes in the performance of the reanalysis before and after each modification. In some cases, the impact of the introduced changes are clear. For example, the quality of the reanalysis changes when different SST products are assimilated. When we switch from a Reynolds SST product to OSTIA, we see an immediate and measurable improvement in the system's performance. We also find that when in-situ T and S profiles from below the ice in the Arctic Ocean are assimilated, the system's performance also improves, and we therefore plead for a continuation of the ITPs after the end of the IPY.

Towards the end of the reanalysis, we introduce a simple ensemble-based bias estimation scheme that detects the seasonal or constant bias in SST and SSH. The implementation of the bias estimation scheme immediately improves the system's performance – not by "correcting" the bias, but by diagnosing it and accounting for it. We demonstrate that the revised MSSH that is constructed using the bias estimation scheme is in better agreement with the independently derived and widely used CNES-CLS09 MDT product.

The evaluation of volume transport through key sections also reveals a correct circulation in the Nordic Seas, which is a necessary prerequisite for modelling the Arctic.

The latest version of TOPAZ includes many changes compared to its predecessor, including a new data assimilation scheme, improvements to many aspects of the configuration of the data assimilation, the assimilation of different observation types, and improvements to the underlying ocean model. Through the pilot reanalysis that we present here, we demonstrate the benefits of these changes and the improvements to the TOPAZ system.

At the same time, verification of the pilot reanalysis clearly identifies the areas for improvement of the system. The water masses in the Arctic in the reanalysis are substantially different from observations from NABOS/CABOS moorings. Specifically, Fig. 16 shows weak or absent Atlantic layer, which points at insufficient Northwards advection through the WSC. While the state of the water masses can be improved by assimilating observations from in-situ profiles, assimilation does not replace a careful model calibration, which can have a major impact on the quality of water masses modelling in the Arctic (Nguyen et al., 2011) even in the abscence of data assimilation.

The multivariate impact of data assimilation has been analysed by comparing the reanalysis and free model with independent data sets. The comparisons show improvements for ice thickness and salinity in the Arctic; and substantial improvement for temperature in the Fram Strait. There are slight improvements for transport estimates across the Svinøy section, but not for the the Barents Sea Opening. Compared with mooring data, there are slight improvements for underwater temperature in the Laptev Sea, but a degradation in the Beaufort Sea. Overall we can believe that this confirms the skill of the EnKF in the Arctic that has been already demonstrated in Lisæter et al. (2003).

Through a 6-year pilot reanalysis, we demonstrate that TOPAZ4 produces a realistic representation of the mesoscale ocean circulation in the North Atlantic, and a realistic representation of sea ice variability in the Arctic. In September 2010, an almost similar TOPAZ4 system was implemented operationally at met.no and produces 10-day forecasts every day. Results from the operational version of TOPAZ4 are available at http://myocean.met.no, and output from the pilot reanalysis are available at http://topaz.nersc.no.

References

Antonov, J., Locarnini, R., Boyer, T., Mishonov, A., and Garcia, H.: World Ocean Atlas 2005 Volume 2: Salinity, NOAA Atlas NESDIS, 62, 182 pp, 2006.

Bentsen, M., Evensen, G., Drange, H., and Jenkins, A. D.: Coordinate transformation on a sphere using conformal mapping, Mon. Weather Rev., 127, 2733–2740, 1999.

Bertino, L. and Lisæter, K. A.: The TOPAZ monitoring and prediction system for the Atlantic and Arctic Oceans, Journal of Operational Oceanography, 2008, 15–18, 2008.

Beszczynska-Möller, A., Woodgate, R. A., Lee, C., Melling, H., and Karcher, M.: A synthesis of exchanges through the main oceanic gateways to the Arctic Ocean, Oceanography, 24, 82–99, 2011.

Bishop, C. H., Etherton, B., and Majumdar, S. J.: Adaptive sampling with the ensemble transform Kalman filter. Part I: theoretical aspects, Mon. Wea. Rev., 129, 420–436, 2001.

Bleck, R.: An oceanic general circulation model framed in hybrid isopycnic-Cartesian coordinates, Ocean Model., 4, 55–88, 2002.

Bonavita, M., Torrisi, L., and Marcucci, F.: The ensemble Kalman filter in an operational regional NWP system: preliminary results with real observations, Q. J. R. Meteorol. Soc., 134, 1733–1744, 2008.

Brasseur, P., Bahurel, P., Bertino, L., Birol, F., Brankart, J.-M., Ferry, N., Losa, S., Remy, E., Schröter, J., Skachko, S., Testut, C.-E., Tranchant, B., Van Leeuwen, P. J., and Verron, J.: Data assimilation for marine monitoring and prediction: The MERCATOR operational assimilation systems and the MERSEA developments, Q. J. R. Meteorol. Soc., 131, 3561–3582, 2005.

Brusdal, K., Brankart, J., Halberstadt, G., Evensen, G., Brasseur, P., van Leeuwen, P. J., Dombrowsky, E., and Verron, J.: An evaluation of ensemble based assimilation methods with a layered OGCM, 40-41, 253–289, 2003.

Burgers, G., van Leeuwen, P. J., and Evensen, G.: Analysis scheme in the ensemble Kalman filter, Mon. Wea. Rev., 126, 1719–1724, 1998.

Canuto, V., Howard, A., Cheng, Y., and Dubovikov, M.: Ocean turbulence. Part II: Vertical diffusivities of momentum, heat, salt, mass, and passive scalars, Journal of Physical Oceanography, 32, 240–264, 2002.

Cardinali, C., Pezzulli, S., and Andersson, E.: Influence-matrix diagnostic of a data assimilation system, Q. J. R. Meteorol. Soc., 130, 2767–2786, 2004.

Cavalieri, D., Parkinson, C., Gloersen, P., and Zwally, H.: Sea ice concentrations from Nimbus-7 SMMR and DMSP SSM/I passive microwave data, CD-ROM. National Snow and Ice Data Center, Boulder, CO, USA, 1999.

Chassignet, E., Hurlburt, H., Smedstad, O., Halliwell, G., Hogan, P., Wallcraft, A., and Bleck, R.: Ocean prediction with the hybrid coordinate ocean model (HYCOM), Ocean Weather Forecasting, pp. 413–426, 2006.

Chassignet, E. P., Hurlburt, H. E., Smedstad, O. M., Halliwell, G. R., Hogan, P. J., Wallcraft, A. J., Baraille, R., and Bleck, R.: The HYCOM (HYbrid Coordinate Ocean Model) data assimilative system, J. Marine Syst., 65, 60–83, 2007.

Compo, G. P., Whitaker, J. S., Sardeshmukh, P. D., Matsui, N., Allan, R. J., Yin, X., Gleason, B. E., Vose, R. S., Rutledge, G., Bessemoulin, P., Brönnimann, S., Brunet, M., Crouthamel, R. I., Grant, A. N., Groisman, P. Y., Jones, P. D., Kruk, M. C., Kruger, A. C., Marshall, G. J., Maugeri, M., Mok, H. Y., Nordli, Ø., Ross,

T. F., Trigo, R. M., Wang, X. L., Woodruff, S. D., and Worley, S. J.: The Twentieth Century Reanalysis Project, Q. J. Roy. Meteorol. Soc., 137, 1–28, 2011.

Cummings, J., Bertino, L., Brasseur, P., Fukumori, I., Kamachi, M., Martin, M., Mogensen, K., Oke, P., Testut, C. E., Verron, J., and Weaver, A.: Ocean data assimilation systems for GODAE, Oceanography, 22, 96–109, 2009.

Dee, D. P., Uppala, S. M., Simmons, A. J., Berrisford, P., Poli, P., Kobayashi, S., Andrae, U., Balmaseda, M. A., Balsamo, G., Bauer, P., Bechtold, P., Beljaars, A. C. M., van de Berg, L., Bidlot, J., Bormann, N., Delsol, C., Dragani, R., Fuentes, M., Geer, A. J., Haimberger, L., Healy, S. B., Hersbach, H., Hólm, E. V., Isaksen, L., Kållberg, P., Köhler, M., Matricardi, M., McNally, A. P., Monge-Sanz, B. M., Morcrette, J.-J., Park, B.-K., Peubey, C., de Rosnay, P., Tavolato, C., Thépaut, J.-N., and Vitart, F.: The ERA-Interim reanalysis: configuration and performance of the data assimilation system, Q. J. R. Meteorol. Soc., 137, 553–597, 2011.

Dorandeu, J. and Le Traon, P. Y.: Effects of Global Mean Atmospheric Pressure Variations on Mean Sea Level Changes from TOPEX/Poseidon, J. Atmos. Ocean. Tech., 16, 1279–1283, 1999.

Drange, H. and Simonsen, K.: Formulation of air-sea fluxes in the ESOP2 version of MICOM, Tech. Rep. 125, Nansen Environmental and Remote Sensing Center, Thormøhlensgt. 47, N-5006 Bergen, Norway, 1996.

Dumont, D., Gratton, Y., and Arbetter, T.: Modeling the dynamics of the North Water polynya ice bridge, J. Phys. Oceanogr., 39, 1448–1461, 2009.

Evensen, G.: Sequential data assimilation with a nonlinear quasi-geostrophic model using Monte-Carlo methods to forecast error statistics, J. Geophys. Res., 99, 10 143–10 162, 1994.

Evensen, G.: The ensemble Kalman filter: Theoretical formulation and practical implementation, Ocean Dynamics, 53, 343–367, 2003.

Ezraty, R., Girard-Ardhuin, F., and Piollé, J.-F.: Sea-ice drift in the central Arctic combining QuikSCAT and SSM/I sea ice drift data – User's manual, Tech. Rep. V2.0, CERSAT-IFREMER, Brest, France, 2006.

Fichefet, T. and Morales Maqueda, M. A.: Sensitivity of a global sea ice model to the treatment of ice thermdynamics and dynamics, J. Geophys. Res., 102, 12609–12646, 1997.

Gammelsrød, T., Leikvin, Ø., Lien, V., Budgell, W. P., Loeng, H., and Maslowski, W.: Mass and heat transports in the NE Barents Sea: Observations and models, J. Mar. Sys., 75, 56–69, 2009.

Gaspari, G. and Cohn, S. E.: Construction of correlation functions in two and three dimension, Q. J. R. Meteorol. Soc., 125, 723–777, 1999.

Girard, L., Weiss, J., Molines, J. M., Barnier, B., and Bouillon, S.: Evaluation of high-resolution sea ice models on the basis of statistical and scaling properties of Arctic sea ice drift and deformation, J. Geophys. Res., 114, C08 015+, 2009.

Halliwell, G.: Evaluation of vertical coordinate and vertical mixing algorithms in the HYbrid-Coordinate Ocean Model (HYCOM), Ocean Modelling, 7, 285–322, 2004.

Houtekamer, P. L. and Mitchell, H. L.: Ensemble Kalman filtering, Q. J. R. Meteorol. Soc., 131, 3269–3289, 2006.

Hunke, E. C. and Dukowicz, J. K.: An elastic-viscous-plastic model for sea ice dynamics, J. Phys. Oceanogr., 27, 1849–1867, 1997.

Hunt, B. R., Kostelich, E. J., and Szunyogh, I.: Efficient data assimilation for spatiotemporal chaos: A local ensemble transform Kalman filter, Physica D, 230, 112–126, 2007.

Ingvaldsen, R., Asplin, L., and Loeng, H.: The seasonal cycle in the Atlantic transport to the Barents Sea during the years 1997–2001, Cont. Shelf Res., 24, 1015–1032, 2004.

Iskandarani, M., Levin, J., Choi, B., and Haidvogel, D.: Comparison of advection schemes for high-order hp finite element and finite volume methods, Ocean Modelling, 10, 233–252, 2005.

Jiang, G. and Shu, C.: Efficient implementation of weighted essentially nonoscillatory schemes J, Comp. Phys, 126, 202–228, 1996.

Johnson, M., Proshutinsky, A., Aksenov, Y., Nguyen, A., Lindsay, R., Haas, C., Zhang, J., Diansky, N., Kwok, R., Maslowski, W., Håkkinen, S., Ashik, I., and de Cuevas, B.: Evaluation of Arctic sea ice thickness simulated by Arctic Ocean Model Intercomparison Project models, J. Geophys. Res., 117, 1–21, 2012.

Kara, A. B., Rochford, P. A., and Hurlburt, H. E.: Efficient and accurate bulk parameterizations of air-sea fluxes for use in general circulation models, J. Atmos. Oceanic Tech., 17, 1421–1438, 2000.

Kwok, R.: Outflow of Arctic Ocean Sea Ice into the Greenland and Barents Seas: 1979–2007, J. Climate, 22, 2438–2457, 2009.

Kwok, R. and Rothrock, D. A.: Decline in Arctic sea ice thickness from submarine and ICESat records: 1958-2008, Geophys. Res. Lett., 36, L15501, doi:10.1029/2009GL039035, 2009.

Large, W. and Pond, S.: Open ocean momentum flux measurements in moderate to strong winds, J. Phys. Oceanogr., 11, 324–336, 1981.

Le Traon, P.-Y. and Ogor, F.: ERS-1/2 orbit improvement using TOPEX/POSEIDON: The 2 cm challenge, J. Geophys. Res., 103, 8045–8057, 1998.

Levitus, S., Antonov, J., and Boyer, T.: Warming of the world ocean, 1955-2003, Geophys. Res. Lett., 32, L02604, doi:10.1029/2004GL021592, 2005.

Lisæter, K., Rosanova, J., and Evensen, G.: Assimilation of ice concentration in a coupled ice-ocean model, using the Ensemble Kalman filter, Ocean Dynamics, 53, 368–388, 2003.

Locarnini, R., Antonov, J., and Garcia, H.: World Ocean Atlas 2005, Volume 1: Temperature., vol. 61, US Dept. of Commerce, National Oceanic and Atmospheric Administration, 2006.

Mauritzen, C., Hansen, E., Andersson, M., Berx, B., Beszczynska-Möller, A., Burud, I., Christensen, K., Debernard, J., de Steur, L., Dodd, P., Gerland, S., Godøy, Ø., Hansen, B., Hudson, S., Høydalsvik, F., Ingvaldsen, R., Isachsen, P., Kasajima, Y., Koszalka, I., Kovacs, K., Költzow, M., LaCasce, J., Lee, C., Lavergne, T., Lydersen, C., Nicolaus, M., Nilsen, F., Nøst, O., Orvik, K., Reigstad, M., Schyberg, H., Seuthe, L., Skagseth, Ø., Skardhamar, J., Skogseth, R., Sperrevik, A., Svensen, C., Søiland, H., Teigen, S., Tverberg, V., and Riser, C. W.: Closing the loop – Approaches to monitoring the state of the Arctic Mediterranean during the International Polar Year 2007-2008, Prog. Oceanogr., 90, 62–89, 2011.

Morison, J., Long, C., and Levine, M.: Internal wave dissipation under sea ice, J. Geophys. Res, 90, 11 959–11 966, 1985.

Ness, B., Counillon, F., and Dumont, D.: Sensitivity of the Arctic and North Atlantic Oceans to the Bering Strait inflow: A modeling study, 310, Nansen Environmental and Remote Sensing Center Technical Report, 2010.

Nguyen, A., Menemenlis, D., and Kwok, R.: Improved modeling of the Arctic halocline with a subgrid-scale brine rejection parameterization, J. Geophys. Res, 114, C11 014, 2009.

Nguyen, A. T., Menemenlis, D., and Kwok, R.: Arctic ice-ocean simulation with optimized model parameters: Approach and assessment, J. Geophys. Res., 116, C04 025, 2011.

Oke, P. and Sakov, P.: Representation error of oceanic observations for ocean data assimilation, J. Atmos. Ocean. Tech., 25, 1004–1017, 2008.

Oke, P. R., Allen, J. S., Mille, r. R. N., Egbert, G. D., Austin, J. A., Barth, J. A. Boyd, T. J., Kosro, P. M., and Levine, M. D.: A modeling study of the three-dimensional continental shelf circulation off Oregon. Part I: model-data comparisons, J. Phys. Oceanogr., 32, 1360–1382, 2002.

Oke, P. R., Brassington, G. B., Griffin, D. A., and Schiller, A.: The Bluelink ocean data assimilation system (BODAS), Ocean Model., 21, 46–70, 2008.

Oke, P. R., Brassington, G. B., Griffin, D. A., and Schiller, A.: Ocean data assimilation: a case for ensemble optimal interpolation, AMOJ, 59, 67–76, 2010.

Oki, T. and Sud, Y. C.: Design of the global river channel network for Total Runoff Integrating Pathways (TRIP), Earth Interactions, 2, 1–37, 1998.

Reynolds, R. and Smith, T.: Improved global sea surface temperature analyses using optimum interpolation, Journal of Climate, 7, 929–948, 1994.

Rio, M. H., Schaeffer, P., Moreaux, G., Lemoine, J. M., and Bronner, E.: A new Mean Dynamic Topography computed over the global ocean from GRACE data, altimetry and in-situ measurements, in: Poster communication at OceanObs09 symposium, pp. 21–25, 2009.

Rodgers, C.: Inverse methods for atmospheres: theory and practice, World Scientific, 2000.

Sakov, P. and Bertino, L.: Relation between two common localisation methods for the EnKF, Comput. Geosci., 15, 225–237, 2011.

Sakov, P. and Oke, P. R.: A deterministic formulation of the ensemble Kalman filter: an alternative to ensemble square root filters., Tellus, 60A, 361–371, 2008a.

Sakov, P. and Oke, P. R.: Implications of the form of the ensemble transformations in the ensemble square root filters, Mon. Wea. Rev., 136, 1042–1053, 2008b.

Sakov, P., Evensen, G., and Bertino, L.: Asynchronous data assimilation with the EnKF, Tellus, 62A, 24–29, 2010.

Schauer, U., Beszczynska-Möller, A., Walczowski, W., Fahrbach, E., Piechura, J., and Hansen, E.: Variation of measured heat flow through the Fram Strait between 1997 and 2006, pp. 65–85, 2008.

Siegismund, F., Johannessen, J., Drange, H., Mork, K. A., and Korablev, A.: Steric height variability in the Nordic Seas, J. Geophys. Res., 112, C12010, doi:10.1029/2007JC004221, 2007.

Skagseth, Ø., Furevi, k. T., Ingvaldsen, R., Loeng, H., Mork, K. A., Orvik, K. A., and Ozhigin, V.: Volume and heat transports to the Arctic Ocean via the Norwegian and Barents Seas, in: Arctic-Subarctic Ocean Fluxes (ASOF), edited by Dickson, R. R., Meincke, J., and Rhines, P., pp. 1–29, Springer, 2008.

Srinivasan, A., Chassignet, E., Bertino, L., Brankart, J., Brasseur, P., Chin, T., Counillon, F., Cummings, J., Mariano, A., Smedstad, O., and Thacker, W.: A comparison of sequential assimilation schemes for ocean prediction with the HYbrid Coordinate Ocean Model (HYCOM): Twin experiments with static forecast error covariances, Ocean Model., 37, 85 – 111, 2011.

Stark, J., Donlon, C., Martin, M., and McCulloch, M.: OSTIA: An operational, high resolution, real time, global sea surface temperature analysis system, in: OCEANS 2007-Europe, pp. 1–4, IEEE, 2007.

Steele, M., Morley, R., and Ermold, W.: PHC: A global ocean hydrography with a high-quality Arctic Ocean, Journal of Climate, 14, 2079–2087, 2001.

Svendsen, E., Kloster, K., Farrelly, B., Johannessen, O., Johannessen, J., Campbell, W., Gloersen, P., Cavalieri, D., and Mätzler, C.: Norwegian remote sensing experiment: evaluation of the NIMBUS 7 Scanning Multichannel Microwave Radiometer for sea ice research, Journal of Geophysical Research, 88, 2781–2791, 1983.

Teague, W. J., Carron, M. J., and Hogan, P. J.: A comparision between the Generalized Digital Environmental Model and Levitus climatologies, J. Geophys. Res., 95, 7167–7183, 1990.

Torn, R. D. and Hakim, G. J.: Performance characteristics of a pseudo-operational ensemble Kalman filter, Mon. Wea. Rev., 136, 3947–3962, 2008.

Wadley, M. and Bigg, G.: Impact of flow through the Canadian Archipelago and Bering Strait on the North Atlantic and Arctic circulation: An ocean modelling study, Q. J. R. Meteorol. Soc., 128, 2187–2203, 2002.

Zalesak, S.: Fully multidimensional flux-corrected transport algorithms for fluids, Journal of Computational Physics, 31, 335–362, 1979.